Structure of a screeching rectangular jet: a stereoscopic particle image velocimetry study

By MEHMET B. ALKISLAR, ANJANEYULU KROTHAPALLI
AND LUIZ M. LOURENCO

Department of Mechanical Engineering, 2525 Pottsdamer Street, Florida A&M University
and Florida State University, Tallahassee, FL 32310, USA
alkislar@eng.fsu.edu; kroth@eng.fsu.edu

The unsteady velocity field generated by an underexpanded jet has been investigated using stereoscopic particle image velocimetry (PIV). A 4:1 aspect ratio converging–diverging rectangular nozzle designed to operate at a fully expanded condition of $M = 1.44$ was used. The nozzle was operated at off-design conditions to generate imperfectly expanded jets with intense screech tones. Phase-locked PIV measurements show the spatial and temporal evolution of the three-dimensional jet with high fidelity. In addition to the globally averaged mean and turbulence velocity field data, the phase-averaged data for the velocity and vorticity fields were also obtained. The turbulence quantities were resolved into contributions from the periodic and random motions. The deformation of the periodic spanwise structures results in the formation of strong streamwise vortices that appear to govern the mixing of the jet. It is shown that the presence of coherent vorticity of significant strength, in addition to the shock cell strength, is largely responsible for determining the screech intensity.

1. Introduction

The primary motivation for the examination of the flow field of a screeching rectangular jet is to provide some guidance towards developing control methods for high-speed jet noise suppression and enhanced mixing for combustion applications. A promising approach for the diffusion of high convective Mach number free shear flows uses the efficient energy transfer between the mean and the turbulent velocity fields caused by global instabilities (Strykowski, Krothapalli & Jendoubi 1996). One such phenomenon, known as 'screech' (Powell 1953) exemplifies the dramatic effect of a self-sustained feedback loop in the global flow response, as shown in figure 1. Unlike isolated shear layers, compressible jets are unstable over a wide range of disturbances for all Mach numbers (Berman & Ffowcs Williams 1970). Consequently, any feedback loop is liable to set up a resonance phenomenon that leads to a self-sustained oscillatory condition common to non-ideally expanded supersonic jets. Powell described the screech phenomenon as being generated by disturbances in the shear layer, which convect downstream and come into contact with a shock cell boundary. This interaction, particularly at the end of a shock cell, results in the generation of intense sound. The sound propagates upstream in the ambient medium, interacts with the incipient shear layer at the nozzle exit and produces a new downstream travelling disturbance that continues the feedback cycle. It is assumed that the sound waves moving in the upstream direction adjacent to the jet are of
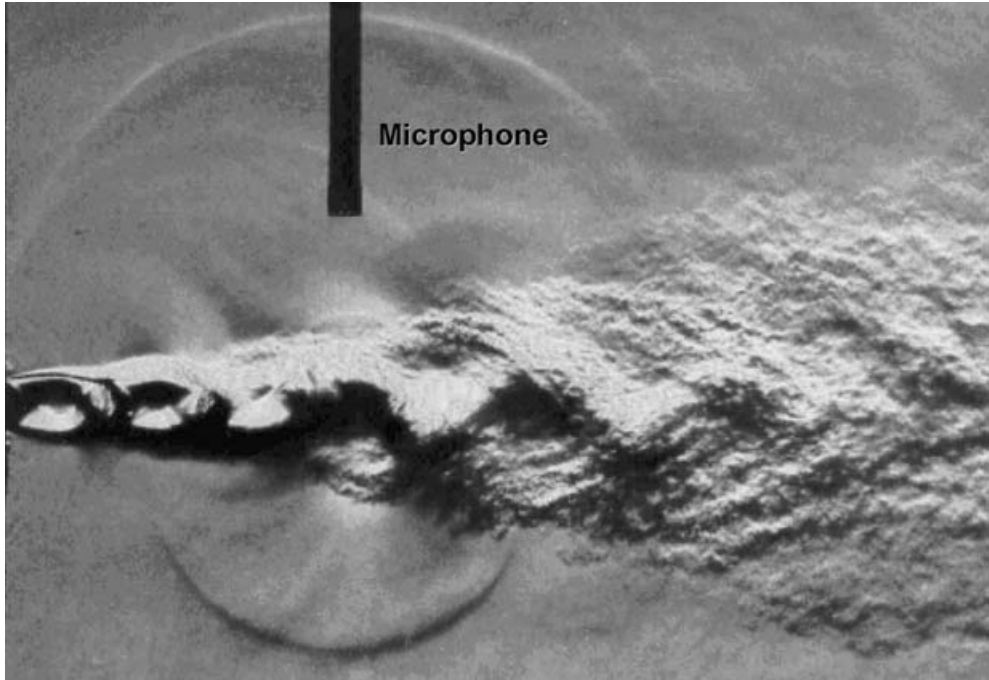
FIGURE 1. Schlieren picture of a screeching rectangular jet issuing from a converging nozzle. Nozzle aspect ratio of 10, nozzle pressure ratio of 3.5.

sufficient strength to affect the stability of the shear layer surrounding the shock cells. Upon reaching the nozzle exit, the acoustic wave gives rise to a localized pressure force, which excites the shear layer. This initial small disturbance usually forms regular undulations, which take on a slightly wavy form (Poldervaart, Wijnands & Bronkhorst 1974). The rapid growth of these undulations results into eddies, which are clearly depicted in figure 1. The instability waves that are part of this process are of convective type and thus have a negligible upstream influence. As a result, the jet could be excited at non-screech frequencies if it is driven by an upstream disturbance of sufficient strength. If an efficient energy transfer mechanism between the undisturbed shear layer and the oscillatory disturbance, in the region covering the first few instability wavelengths, is devised, the resulting motion of the jet could be as violent as that observed for a screeching jet (Poldervaart 1976). Indeed, using flow-induced cavity resonance at the nozzle exit to excite the shear layer, Yu & Schadow (1994) were able to show that the initial shear-layer growth rate can be increased by a factor of nearly three at a high convective Mach number ($M_c = U_j/(a_1 + a_2)$; where U_j is the mean velocity of the jet and a_1 and a_2 are the speed of sound in the jet and the ambient medium respectively) of 1.4.

Since the pioneering work of Powell, many theoretical and experimental investigations have been carried out to elucidate the features of screech tones (see the review article by Raman 1998).

It is commonly believed that the eddies seen in flow-visualization pictures are a manifestation of the shear-layer instability process, and correspond to the nonlinear stage of the growth in which the infinitesimal waves grow and distort to form vortices. The linking of the instability process to the formation of large-scale coherent structures

has been firmly put in place by Morris, Giridharan & Lilley (1990). Modelling the large-scale coherent structures as a superposition of instability waves, they predicted the experimentally observed properties of two-dimensional compressible shear layers without the inclusion of any empirical constants. The rapidly growing instability waves, representing the flapping mode in a rectangular jet, evolve into the intense coherent eddies, as seen in figure 1. An accurate prediction of the screech frequency can be made given the knowledge of the shock cell structure mean flow characteristics coupled with the tools of stability analysis (Tam 1988). However, the prediction of screech tone amplitude remains elusive and the results presented in this paper may provide some guidance in this direction.

A marked feature of the picture taken at a given phase within a screech cycle and shown in figure 1 is the simultaneous presence of a nascent vortical structure and the birth of a cylindrical acoustic wave at the end of the third shock cell (top shear layer). Based on similar flow-visualization images and other related work, it was hypothesized (Krothapalli, Baganoff & Hsia 1983) that the screech tone amplitude is related to the strength of the coherent vorticity in the vortical structure and shock strength at the end of the shock cell. This suggestion was primarily based on qualitative observations without supporting measurements. Recent numerical investigations by Manning & Lele (2000) have revealed the dependence of the sound-field intensity on the shear-layer disturbance amplitude and the shock strength. The model involves the two-dimensional interaction of shear-layer vortices with an isolated region of the jet shock cell structure. Their results clearly indicate that the radiated acoustic pressure amplitude is closely related to the instability wave amplitude. Having established that the instability wave amplitude is closely tied to the evolution of large-scale vortices, a strong case may then be made that their strength largely determines the amplitude of the radiated sound. Hence, a description of the large-scale structure dynamics constitutes a significant part of the present paper. It is probably fair to say that not much has been learned directly about the dynamics of these structures from flow-visualization studies.

The variation of the screech tone amplitude with nozzle pressure ratio typically assumes a parabolic shape (Krothapalli *et al.* 1986; Krothapalli & Strykowski 1996). Using a shallow water table to simulate the sound radiation from a screeching rectangular jet, Brocher & Makhsud (1997) have shown that the static pressure gradient at the end of the third shock cell follows a parabolic variation with a parameter equivalent to the jet Mach number similar to the screech amplitude trends shown by Krothapalli *et al.* (1986). Hence, they established a strong link between the screech tone intensity and the static pressure gradient at the location of screech sound generation. Given that intense local concentrations of vorticity are often accompanied by high values of pressure gradients (Prandtl 1952), it is consistent to assume that higher-strength vortical structures are present at maximum screech intensity. Therefore, a study the role of the vortical structures in determining the screech tone amplitude deserves attention.

The paper is organized as follows. In §2, the experimental procedures, which also include a brief description of the phase-locked stereoscopic PIV system set-up, are explained. Section 3.1 addresses the sound field characteristics. The global mean flow is described in §3.2 which addresses the growth rates of the jet in major and minor axes planes. The properties of the periodic spanwise large-scale vortical structures and the development of the streamwise structures are discussed in §3.3. Finally, §3.4 presents the characteristics of coherent and chaotic turbulence intensity fields.

2. Apparatus, instrumentation and procedures

The experiments were conducted in the blowdown compressed-air facility of the Fluid Mechanics Research Laboratory at the Florida State University. A high-displacement reciprocating air compressor drives the facility; it is capable of supplying air at a maximum storage pressure of 14 MPa. Large storage tanks provide a total capacity of 10 m^3. After leaving the storage tanks, the air can be heated by passing through an array of resistive tank heaters having a maximum power output of 450 kW and capable of achieving stagnation temperatures up to 700 K. The jet with an exit Mach number, $M_j = 1.69$, used in this study can be run continuously for about 30 min.

The blowdown facility was fitted with a rectangular nozzle having an exit aspect ratio of 4:1. The dimensions of the nozzle in the exit plane measured, height, $h = 10$ mm, and width, $w = 40$ mm. The contour of the short dimension of the nozzle was generated using the method of characteristics for a design Mach number of 1.44. The walls of the long dimension of the nozzle were kept parallel downstream of the throat. The circular dimension of the connecting pipe (diameter = 76 mm) upstream of the throat was blended to facilitate a smooth transition to the rectangular cross-section. To avoid problems of condensation associated with the humid Florida air, the jet was operated at a stagnation temperature of 335 K. The plenum pressure and temperature can be maintained steady by two pneumatic valves and electrical heaters with automatic controllers. During the present experiments, the pressure was kept at its nominal value within a variation of ± 2 kPa. The total temperature was kept at the nominal value of 336 ± 2 K with a relative error of 0.6%. The resulting error in the velocity, for $M_j = 1.69$, is ± 3 m s^{-1} (less than 1%).

The mean exit velocity profile with laminar boundary layers was a top-hat as the jet was exhausted into a quiet surrounding at ambient conditions. The jet exit Reynolds number based on the nozzle exit height and the mean exit velocity is 4.3×10^5. A Cartesian coordinate system (X, Y, Z) was chosen with its origin located at the centre of the nozzle exit plane and with the X-axis oriented along the centreline of the jet, Y- and Z-axes are oriented along the short and long dimensions, respectively (see figure 4). The measurements are confined to the central plane (the (X, Y)-plane) of the jet containing the small dimension of the nozzle and (Y, Z)-planes at selected locations downstream of the nozzle exit.

Submicron (~ 0.3 μm) oil droplets generated using a modified Wright nebulizer provided the necessary seeding for the jet, whereas the ambient air was seeded with smoke particles ($1 \sim 5$ μm in diameter) produced by a Rosco fog generator. Seeded air output is mixed with the main air-supply stream in the inlet pipe at 1.25 m upstream of the nozzle. Although the particles in the jet core were exposed to relatively weak compression and expansion of the flow within the shock cells, very little particle lag was noticed in the measurements, as it will be shown in §3. The larger particles in the ambient medium that are entrained into the jet remain confined mostly to the subsonic region of the flow and do not pose a lag problem.

2.1. *Particle image velocimetry (PIV)*

Non-intrusive measurements of the velocity field were made using stereoscopic particle image velocimetry (PIV). A detailed discussion of the application of the stereoscopic PIV technique to supersonic jets is given in Alkislar, Lourenco & Krothapalli (2000).

The Kodak ES1.0 CCD cameras used to capture the images have a resolution of $1008(H) \times 1018(V)$ pixels with size of 9×9 μm, and a maximum frame rate of 30 Hz. The camera was equipped with a 58.37 mm focal length lens that was specifically designed for the wavelength of the laser light. A microcomputer, with two Pentium II

CPUs, controlled the camera, and was capable of acquiring up to 128 image pairs at the maximum camera framing rate. To illuminate the flow field, a frequency doubled Nd-Yag laser with dual cavity (Spectra-Physics PIV-400) was used. The time, Δt between the two laser pulses was kept between 1 and 1.5 μs.

In order to obtain velocity data with high spatial resolution, a novel-processing algorithm was employed (Lourenco & Krothapalli 2000). Velocity information is obtained from a pair of single exposed PIV images by subdividing the images into subimages (interrogation area) and quantifying the average spatial shift of particles from one image to the other by statistical correlation techniques. To eliminate the errors due to the finite interrogation size, e.g. loss of pairing, image truncation, velocity and seeding gradient in the interrogation region, a masking method is enabled. In this method, the particles in the interrogation area are detected by a threshold that is found from the average gradient for each region being analysed. The mask in the method is a map of the interrogation area filled with ones at the locations where the particle image is detected and zeros otherwise. Zeros are also assigned to the particle locations at the edges of the interrogation area. This operation results in the elimination of the background noise due to the reflections and parasite illumination, and the effect of particle truncation, also increasing the signal level in the correlation peak. The application of the mask eliminates the bias effect seen in the standard fast Fourier transform (FFT) correlation and results in a significant reduction of scatter.

In addition, to eliminate the errors due to image pairing loss originating from correlating two fixed regions, a scheme is used in which the maximum number of pairings between the two regions is sought by correlating the smaller interrogation window with a larger window. To accommodate the size difference in the FFT, the smaller region is padded with zeros to form the same size as the larger region. This adaptive window technique reduces the scatter of the data even further.

A high-resolution feature is implemented to account for the velocity and seed density gradient effects that occur in practical PIV recordings. During the mask operation, the particle detection feature also generates a list of the centre of mass position, area and form factor of each particle image. Then, a particle image pairing procedure is applied based on the group displacement. In this procedure, a direct spatial domain correlation is performed to find the displacement for the maximum correlation. Subpixel resolution is achieved by means of a Gaussian interpolation procedure. The measurement position equal to the half-distance between the centres of mass of corresponding images is assigned to each of the measured displacements as displacement position with a second-order evaluation. The error associated with each measurement is minimized by using a least-squares fitting algorithm. In order to maintain the second-order accuracy a second-order polynomial was used as,

$$\boldsymbol{u} = \boldsymbol{a}x^2 + \boldsymbol{b}x + \boldsymbol{c}y^2 + \boldsymbol{d}\,y + \boldsymbol{e}\,xy + \boldsymbol{f}. \tag{1}$$

The sizes of the interrogation regions are dynamically adapted during the computation to ensure that there are at least ten values in the displacement-positions list. The marked advantage of this approach is that the field is described at any point with second-order accuracy, including the derivatives that are found by differentiating the previous equation. The error minimization approach maintains the order of the accuracy and provides a means for an accurate evaluation of the field derivatives. Although an unstructured grid is used for calculating the velocity, for ease of presentation, the velocity field is usually presented at regular intervals. Detailed discussion of the processing technique and comparison with standard PIV algorithms can be found in Lourenco & Krothapalli (2000).
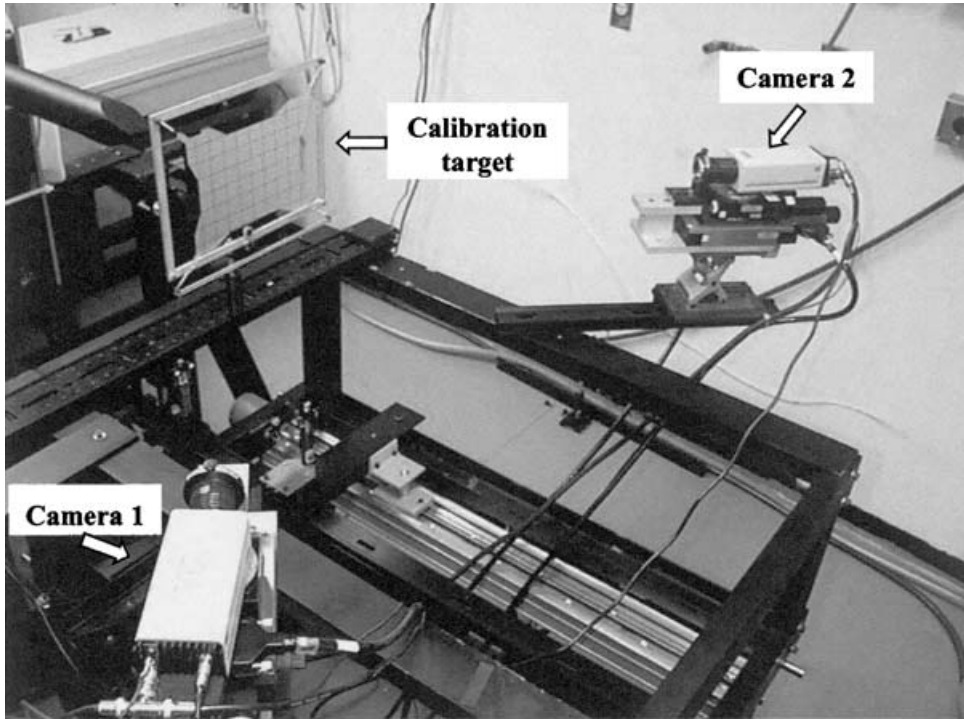
FIGURE 2. The PIV set-up.

Considering all the effects, an error of 0.03 pixels is conservatively estimated in the displacement calculation. Time delay between the two pulses is chosen to give maximum displacement in the flow field of not less than 6 pixels, giving a relative error of 0.5%. For the jet velocity of 495 m s^{-1} it corresponds to ± 2.5 m s^{-1}.

Because the PIV measurements are restricted to a limited region, to cover the entire jet, it was necessary to divide it into several measurement zones. These zones may have different sizes to cover the regions of interest. In addition, they overlap to ensure the coverage of the whole flow field and proper match. At the edges of the zones, data can be more erroneous because of unnoticed focusing variations and/or magnification limitations. In order to minimize these effects, a weighted averaging method is used to combine the data at the overlapping regions of the different zones. At the beginning of the overlapping region, the first zone has the full weighting of one and the second zone starts with a value of zero weighting at the edge. While moving towards the end of the overlap, the weighting in the first zone decreases linearly to zero and at the second zone it increases to one. The same procedure is repeated for every overlapping region. This procedure minimizes the zone-edge problems and mismatches by decreasing the weighting in those regions. In this fashion, a smooth variation of the velocity contours is obtained after the combination of four regions, each with a measurement area of 65 mm in height and 105 mm in length. The overlapping region covers 30 mm in length.

2.1.1. *PIV set-up*

As shown in the figure 2, two cameras are positioned at an angle with respect to the measurement plane to obtain the stereo-view. In this arrangement, the Scheimpflug condition (for which measurement plane, lens plane and image planes coincide along
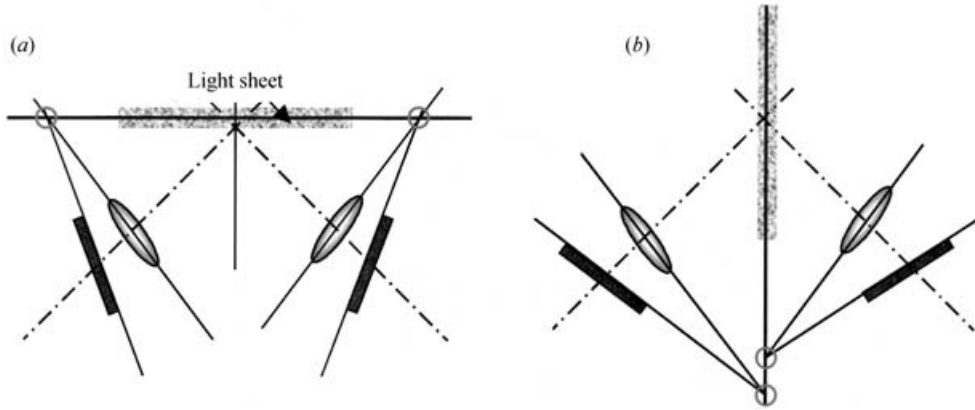
FIGURE 3. Different modes of viewing for stereoscopic imaging with the Scheimpflug condition. (*a*) Same side imaging, (*b*) opposite side imaging.

a line, as illustrated with circles at the intersection of three planes in figure 3) ensures that uniform focus is obtained in the image plane. In practice, this condition is obtained by rotating the camera body with respect to the lens plane. In order to attain the precise focusing of the particles in the laser sheet, two motors with remote control were assembled with the camera and lens as pictured. Special attention is given to make sure that the camera sensor is positioned on the axis of rotation and its midpoint is aligned with the optical axis of the lens so that the rotation of the camera will not cause a translation in the field of view. The angle between the axes of the two camera views is set at approximately 90°, which gives the maximum accuracy in the three-dimensional reconstruction (Alkislar 2001). A calibration procedure ensures that the views from each camera are free from perspective effects, and it provides the necessary correspondence between the coordinate positions of each camera view so that the three-dimensional velocity field is accurately reconstructed. Two different types of imaging modes, as shown in figure 3, are used, based on the flow field of interest. The same side imaging mode is particularly used for cross-plane (Y, Z) measurements. For a more detailed discussion on stereoscopic PIV, see Alkislar (2001).

2.2. *Pressure measurements*

Total and static pressure surveys were performed along the centreline of the jet and at several downstream locations in the central minor axis plane. Data obtained from these two different probes were combined to calculate the Mach number distribution. The accurate positioning of the probes in the flow field was accomplished by a three-axis traverse mechanism. Each axis has its own motion controller unit made by Compumotor, and controlled by a digital computer. The computer is a Dell 386 personal computer with an analogue data acquisition board. The absolute position of the traverse can be stored and maintained remotely to within 2 μm. This is also the minimum step size of the system.

For the total and static pressure measurements, two different probes were used. The total and static probe output were connected via 3.175 mm diameter nylon tube to a Validyne model DP-15 pressure transducer with operating ranges of 1 MPa and 70 KPa, respectively. Output voltage of the transducers was adjusted to give 10 V at the maximum pressure. The voltage signal was digitized and acquired at the rate

of 512 samples per second. Then the average of the 512 samples was written to an ASCII data file along with the three coordinate positions of the probe.

The static probe was manufactured according to the design of Pinckney (1975) and is described in detail in Wishart (1995). Considerable attention was given to ensure that the probes were oriented parallel to the nozzle centreline and this was accomplished with the help of a 10 mW He-Ne continuous wave laser.

2.3. *Acoustic measurements*

Acoustic measurements were performed to identify the nature of screech tone at off-design conditions. In this study, the Bruel & Kjaer (B & K) acoustic measurement system was used. The system comprises of a quarter-inch condenser microphone (model 4136), a pre-amplifier (model 2633) and a Nexus conditioning amplifier with an onboard bandpass filter. The signal was filtered in the frequency range between 20 Hz and 100 kHz. Each data set comprises of 320 k sample points acquired with a sampling frequency of 250 kHz. This acquisition frequency allows us to compute frequency spectra up to 100 kHz without violating the Nyquist criteria. Standard FFT methods were used to obtain the power spectra and sound pressure level (re: 20 μPa). A rectangular filtering window was used in the FFT calculations. The spectra have a resolution of 60 Hz. In the decibel range of interest in this investigation, which is larger than 120 dB, the maximum calculated error considering only the microphone characteristics is within ± 1 dB. Several repetitions of the same experiment on the same set-up also yielded a maximum of ± 1 dB error.

2.4. *Phase locking technique*

The time evolution of the coherent motion was obtained using the phase-averaging technique. Following the work of Reynolds & Hussain (1972), and Cantwell & Coles (1983), any flow variable, $q(\boldsymbol{x}, t)$, can be decomposed into two components as shown in equation (2).

$$q(\boldsymbol{x}, t) = \langle q(\boldsymbol{x}, \tau) \rangle + q''(\boldsymbol{x}, t), \tag{2}$$

where, $\langle \ \rangle$ is the average at a constant phase (which is also commonly used as the phase average), $q''(\boldsymbol{x}, t)$ is the random component and τ is the phase delay within the period of one screech cycle. Then, the average at a constant phase is given by the following expression.

$$\langle q(\boldsymbol{x}, \tau) \rangle = \bar{q}(\boldsymbol{x}) + \tilde{q}(\boldsymbol{x}, \tau), \tag{3}$$

where $\bar{q}$ is the global mean and $\tilde{q}$ is the periodic mean component.

In the present experiment, the average at a constant phase was obtained using the following equation.

$$\langle q(\boldsymbol{x}, \tau) \rangle_m = \frac{1}{N_m} \sum_{i=1}^{N_m} q(\boldsymbol{x}, t_i + \tau_m), \tag{4}$$

where N_m is the number of samples acquired at phase τ_m from the reference time t_i. The reference time is obtained from the signal of screech sound measured by a microphone located in the vicinity of the nozzle exit. Preliminary PIV investigations suggested that $N = 30$ samples were sufficient to achieve statistical convergence of the velocity field. A maximum mean value error of 5% of the maximum velocity with 90% confidence level was considered as a converged velocity field at a constant phase. The global mean is obtained using the following expression:

$$\bar{q}(\boldsymbol{x}) = \frac{1}{M} \sum_{m=1}^{M} \langle q(\boldsymbol{x}, \tau) \rangle_m. \tag{5}$$
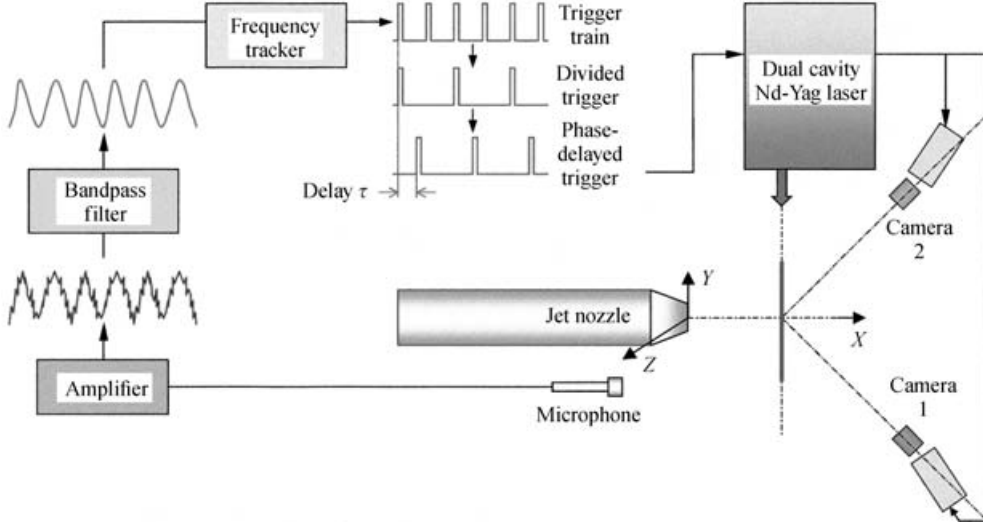
FIGURE 4. The phase locking set-up.

The global mean values were found from the mean of the phase-averaged quantities as shown in (5) where M is the number of phases. In this study, $M = 16$ was used, therefore the screech cycle was sampled at $22.5°$ intervals. The phase average velocity field was obtained using 35 samples, while the global mean velocity field was obtained using 560 samples.

Once the global mean is calculated, the fluctuating component can be obtained from (3). The second-order correlations are calculated using the following equations,

$$\langle q''r'' \rangle_m = \langle qr \rangle_m - \langle q \rangle_m \langle r \rangle_m, \tag{6}$$

$$\overline{\tilde{q}\tilde{r}} = \overline{\langle q \rangle \langle r \rangle} - \bar{q}\bar{r}, \tag{7}$$

$$\overline{qr} = \bar{q}\bar{r} + \overline{\tilde{q}\tilde{r}} + \overline{q''r''}, \tag{8}$$

and the total Reynolds stresses (conventional stresses obtained by classical Reynolds averaging) are simply the addition of the global fluctuating and global random components as,

$$\overline{q'r'} = \overline{\tilde{q}\tilde{r}} + \overline{\langle q''r'' \rangle} = \frac{1}{M} \sum_{m=1}^{M} (\tilde{q}\tilde{r} + \langle q''r'' \rangle)_m. \tag{9}$$

2.4.1. *Phase locking set-up*

A diagram of the set-up for the phase locked PIV measurements is shown in figure 4. As shown in the figure, a microphone appropriately placed near the nozzle exit provides the screech sound signal. After conditioning with a bandpass filter, the screech signal is used as an input to a frequency-tracking and pulse-generating unit. This custom-made unit is capable of tracking signals with frequencies between 400 Hz and 12 kHz. It generates the pulse trigger train that has the same phase as that of the input signal. Next, it divides the trigger signal up to 10 000 times so it corresponds to the frequency of the laser and the camera. Finally, it delays the divided signal up to 0.1 s with 0.1 μs increments, in order to generate the necessary phase pulse for the synchronized camera and laser strobe. All time delays are realized with an accuracy of ± 1 ns.
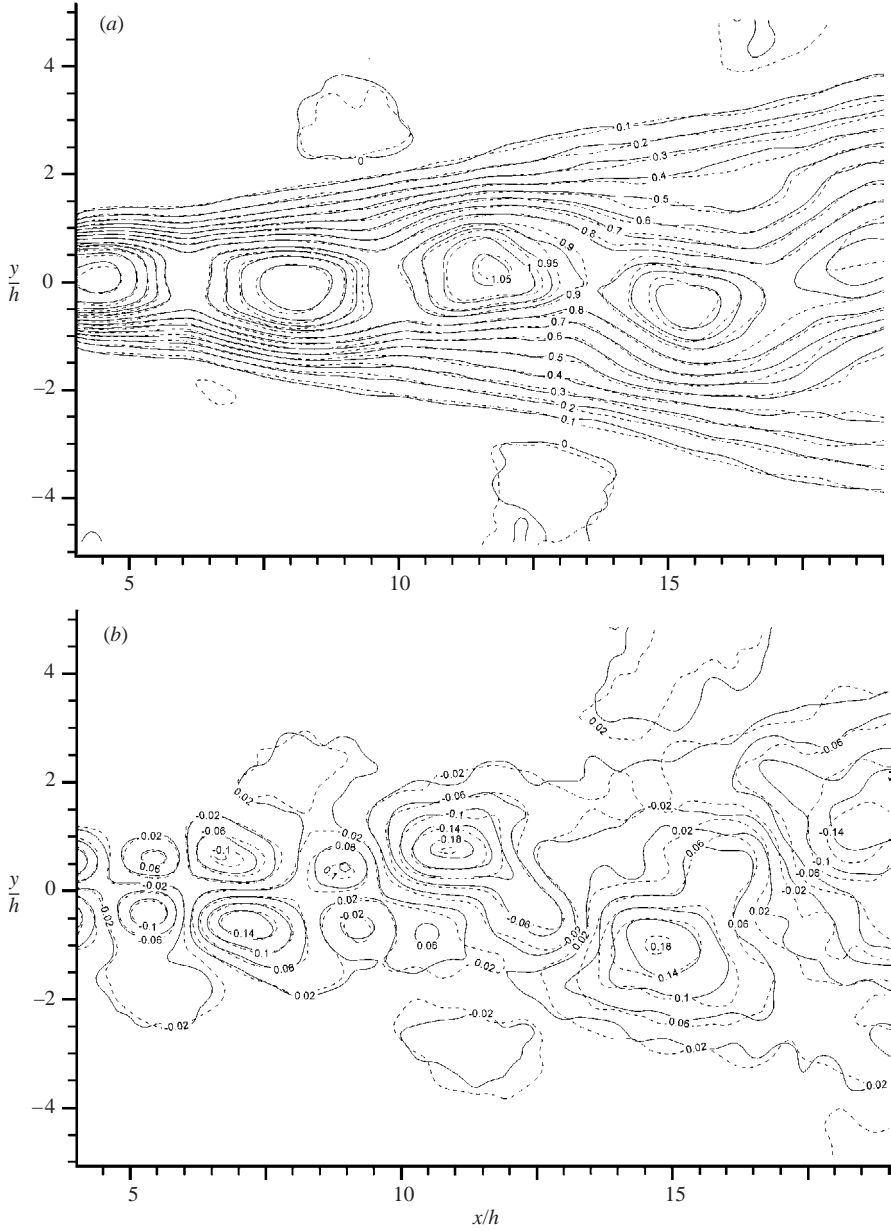
FIGURE 5. Comparison of (a) axial velocity and (b) transverse velocity contours
for —, phase 90° and ---, reflected phase 270°.

2.4.2. *Validation of phase-locked measurements*

In order to increase the resolution in time, the phase-locked measurements were
made in half of the screeching cycle and the reflection of this data is used for the
remaining half of the cycle. To validate this idea, PIV data acquired with 180° phase
delay are compared. A typical result is shown in figure 5(a), where the normalized
axial velocity field in phase 90° is drawn in solid lines and it is compared to the data
of reflected phase 270° in dashed lines. An excellent match is obtained between the
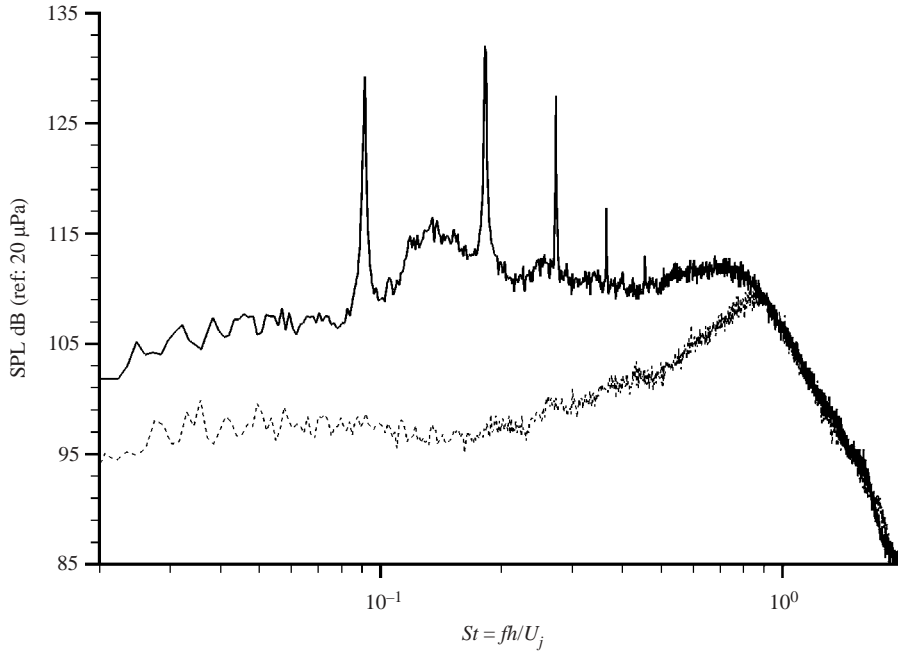
FIGURE 6. Near-field spectrum of a microphone signal. Measurement radius, $R/h = 25$; nozzle inlet angle, $\chi = 90°$. —, $M_j = 1.68$; ---, 1.44.

two sets of data in all the velocity ranges. A similar comparison is made in figure 5(*b*) for the normalized transverse velocity data for which the velocity range is six times lower. Each velocity field corresponding to one phase is an average of about 35 samples.

3. Results and discussion

3.1. *Near-field sound characteristics*

A typical near-field spectrum of the microphone signal is shown in figure 6. The microphone was positioned at a distance of $R = 25h$ ($y/h = 25$) normal to the jet axis (nozzle inlet angle, $\chi = 90°$) in the central (X, Y)-plane of the jet. The abscissa is the Strouhal number, defined based on the nozzle height and the fully expanded jet velocity, while the ordinate shows the sound pressure level (SPL) in decibels. The presence of the screech tone is clearly identifiable with the distinct peaks corresponding to the fundamental frequency and its harmonics. The amplitude of the first harmonic is comparable to that of the fundamental. For comparison purposes, the spectra corresponding to the nozzle design condition of $M_j = 1.44$ is also included in the figure. As expected, the absence of screech tones at the design condition is evident in the spectrum along with lower SPL levels of almost 10 dB for $St < 0.8$.

The variation of the Strouhal number corresponding to the fundamental screech frequency, with the fully expanded Mach number is shown in figure 7. A slight but clear jump in the Strouhal number is observed when the operating condition of the jet is changed from the overexpanded to the underexpanded condition. Such a jump is generally attributed to a change in the oscillatory mode of the jet (Raman 1998) – a shift from the varicose (symmetric) mode to the flapping (antisymmetric) mode. However, examination of our PIV data indicates that the flapping mode,
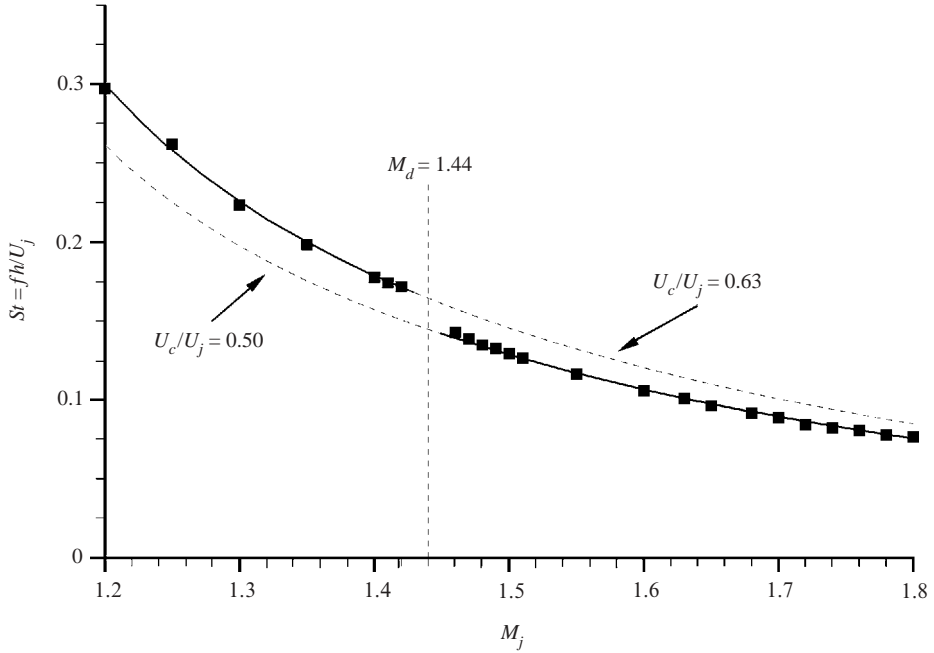
FIGURE 7. Screech tone Strouhal number variation with fully expanded jet Mach number. ■, measured; —, Tam (1988); $AR = 4$.

similar to that seen in figure 1, remains dominant in both the overexpanded and the underexpanded conditions. The most important parameters that determine the frequency variation with the nozzle pressure ratio (NPR) are: the fully expanded jet Mach number; the shock cell length; the convection velocities of the large-scale disturbances in the shear layer; and the acoustic wave speed in the ambient medium (Powell 1953). The solid line in the figure is obtained using Tam's formula (Tam 1988); with the measured convection velocities of large structures inserted in it. The phase-resolved flow-field data were used to determine the convection speed of the large structures present in the shear layer (§ 3.3). The velocity was found to be higher in the overexpanded jet ($U_c/U_j = 0.63$) than in the underexpanded jet ($U_c/U_j = 0.5$). Upon comparing the data with the prediction formula, it appears that the discontinuity in the variation of St with M_j can be attributed to the different convection velocities of the large structures in the overexpanded and the underexpanded conditions.

The screech tone amplitude variation with the fully expanded jet Mach number is shown in figure 8. Guided by previous observations (Krothapalli *et al.* 1986; Krothapalli & Strykowski 1996), a second-order polynomial is fitted through the data for each of the two different operating regimes: overexpanded and underexpanded. The parabolic nature of the screech intensity variation with Mach number, observed earlier, is further confirmed by these measurements.

3.2. *Global mean flow*

The global jet behaviour is first examined through the detailed measurements of the velocity distributions. The time-averaged velocity and vorticity fields are a manifestation of the dynamics of the large-scale vortical structures and their interactions with random turbulence.
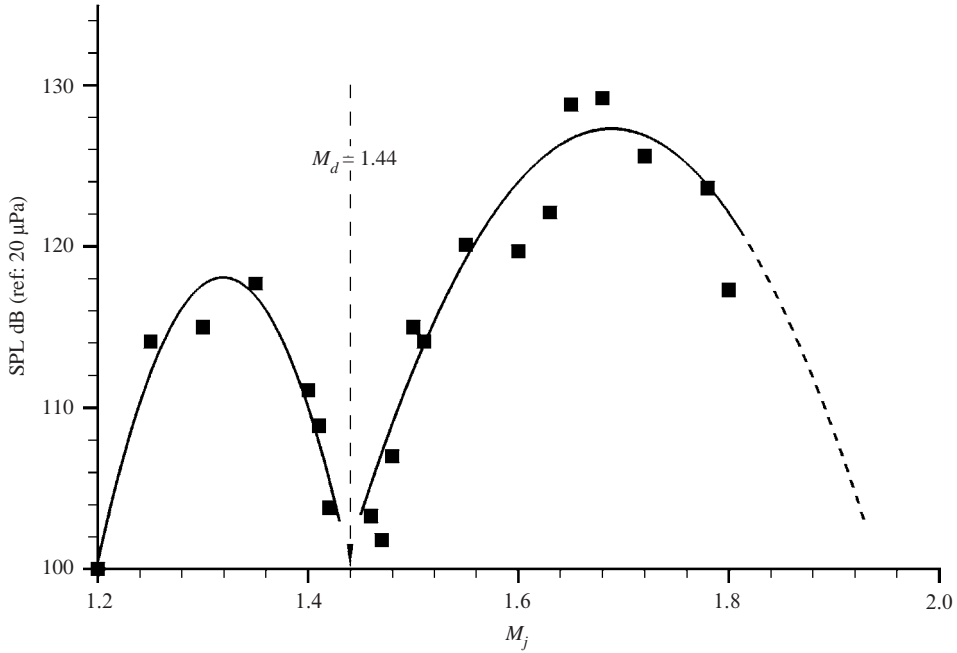
FIGURE 8. Variation of the screech tone amplitude with fully expanded jet Mach number. ■, measured; —, second-order fit.

3.2.1. *Mean axial velocity distributions*

The cross-plane mean velocity fields at different downstream locations, as shown in figure 9, best capture the three-dimensional features of the jet evolution. The velocity distributions are represented by the contours of the axial mean velocity magnitude normalized by the fully expanded jet velocity ($U_j = 495$ m s^{-1}). The axis-switching phenomenon, commonly observed in low-speed jets (Krothapalli, Baganoff & Karamcheti 1981), is vividly depicted here. While the long dimension of the jet column is aligned with the major axis at the nozzle exit, at an axial distance of $25 h$, it clearly aligns itself with the minor axis. An increased growth rate in the minor axis plane produces a jet width at $x/h = 25$ that is about three times larger than an ideally expanded jet. In this study, owing to the absence of self-excitation, the ideally expanded jet grows normally and does not show the commonly observed axis-switching phenomenon. It will be shown later that the axis switching observed presently is related to the generation of strong streamwise vortices whose origins are intimately connected to the dynamics of the coherent spanwise vortices.

The faster growth rate in the minor axis plane is further examined using the velocity field measurements in the central (X, Y)-plane. The normalized axial mean velocity magnitude contours for the screeching jet in the minor axis plane are shown in figure 10. The distinctive character of an underexpanded jet with the classical shock cell structure is clearly seen with six cells. Also shown in the figure is the supersonic region of the jet, whose boundary is marked by a solid line drawn through the locus of $M_j = 1$ points in the flow field. This region extends from the nozzle exit to about $x = 28 h$. The cyclical variation of the velocity field is typical of underexpanded jets. Considering stationary sources at the end of the shock cells and the phasing between adjacent sources, Powell (1953) derived a formula for the screech tone frequency that
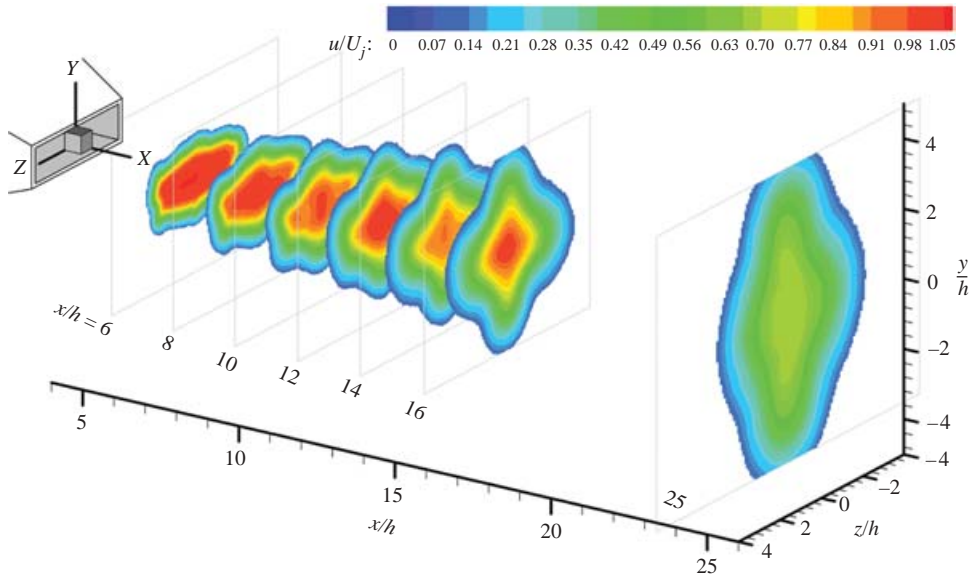
FIGURE 9. Mean axial velocity distribution at several transverse locations.
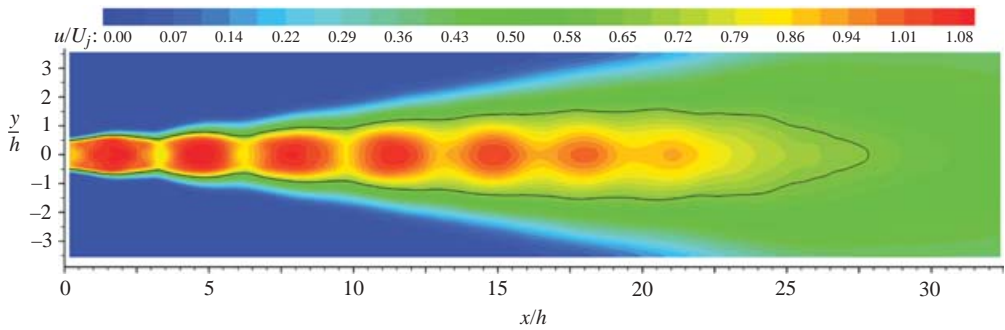

FIGURE 10. Normalized mean streamwise velocity contours in the central minor axis plane.

is in reasonable agreement with the experimental results. The number of sources used in his calculation depend upon the number of shock cells, which, in turn, is primarily related to the strength of the underexpansion at the nozzle exit. The shock cell spacing also plays a prominent role in the Powell or Tam formula for calculating the screech frequency.

The variation of the axial mean velocity along the centreline is given in figure 11. Also included in the figure is the velocity data derived from total and static pressure measurements and assuming isentropic relations. In spite of rapid accelerations and decelerations encountered by the seeding particles within the shock cells, the velocity data obtained using PIV is in excellent agreement with that derived from pressure measurements. Hence, the particle lag typically seen in shock-containing supersonic flows is not of much concern in this experiment. Any deviations from the two sets of data is mostly due to the isentropic assumption used in deriving the velocity from pressure measurement in the downstream regions of the jet, where viscous effects begin to influence the flow.
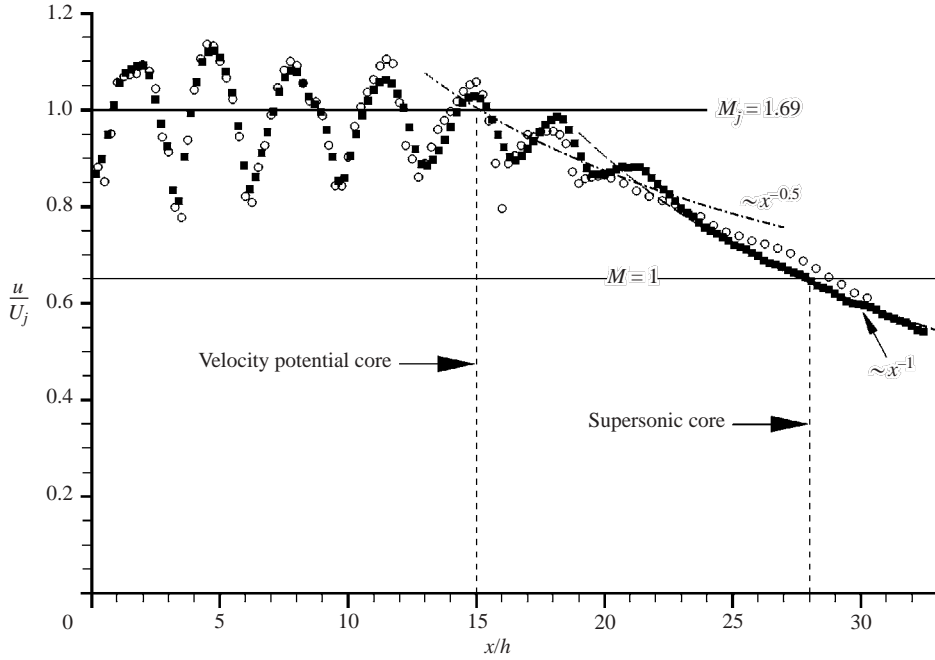
FIGURE 11. Downstream variation of the mean centreline axial velocity. ○, probes; ■, PIV; —·—, curve fit ($\sim x^{-0.5}$); ---, curve fit ($\sim x^{-1}$).

The velocity shown in figure 11 is normalized with the fully expanded jet velocity corresponding to $M = 1.69$ (i.e. $U_j = 495$ m s^{-1}). The extent of the sonic region is also noted in the figure. Usually, the decay of the centreline velocity of an incompressible rectangular jet shows two distinct regions: the two-dimensional region, where the centerline velocity $U_c \propto x^{-0.5}$ followed by an axisymmetric region where $U_c \propto x^{-1}$. Because of rapid diffusion of the jet in the (X, Y)-plane, the extent of the two-dimensional region is almost non-existent in the present case. Beyond about $x = 22\,h$, the centreline velocity seems to decay in a similar way to an axisymmetric jet.

The diffusion of the jet is quantified by the variation of the jet half-velocity widths, with downstream distance as shown in figure 12. The half-velocity width is defined as the distance from the centreline of the jet to the point where the mean velocity is equal to half of the fully expanded jet velocity. The data are obtained from the mean velocity field shown in figures 9 and 10. Also included in the figure are the data of an ideally expanded jet at $M = 1.44$. Like incompressible jets, the ideally expanded jet spreads linearly with downstream distance, albeit with a slower spreading rate. The half-velocity width variation can be represented by

$$y_{0.5} = k(x - x_0), \qquad (11)$$

where the slope k is calculated as 0.065 in the minor-axis plane and 0.058 in the major-axis plane for an ideally expanded jet. The value of k is in accordance with previous measurements of Krothapalli *et al.* (1986). Unlike incompressible jets, the ideally expanded supersonic rectangular jet does not switch axes, as can be inferred from the results shown in figure 12.

The minor-axis plane growth rate of the screeching jet shows two distinct slopes. The faster growth of the jet ($k = 0.11$) in the region from $x/h = 5$ to $x/h = 20$ is
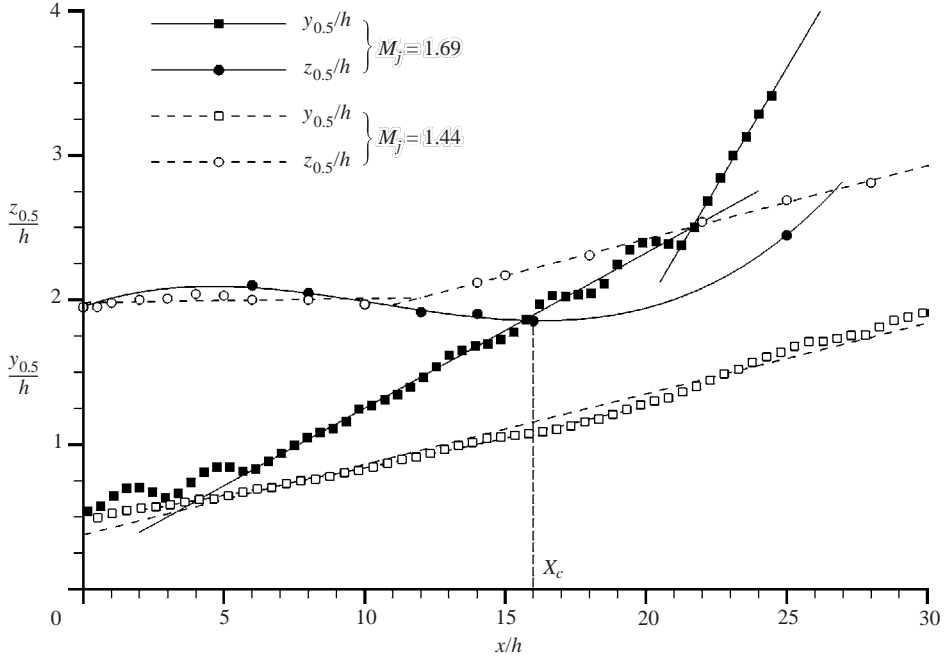
FIGURE 12. Jet spread in major- and minor-axes planes.

due to the self-excitation of the shear layer which results in the organized vortical structures seen in figure 1. A further increase in the growth rate ($k = 0.33$) seen beyond $x/h > 21$ is due to the presence of strong streamwise vortices that are formed from the three-dimensional deformation of the spanwise vortical structures, as will be discussed in §3.3. The cross-over point, X_c at $x/h = 16$ is in accordance ($X_c/h \sim 4 \, \text{AR}$; $\text{AR} = $ nozzle aspect ratio) with the data of incompressible rectangular jets (Krothapalli *et al.* 1981). The half-width in the major-axis plane does not vary significantly. Hence, the jet dynamics is mostly governed by the flow evolution in the minor-axis plane with vigorous mixing processes.

3.2.2. *Mean transverse velocity distributions*

Figure 13 shows the transverse velocity in the cross-planes (Y, Z) at three different downstream locations. The uniformly scaled velocity vector fields are superimposed with the contours of the normalized out-of-plane component of the vorticity ($\omega_x = \partial w/\partial y - \partial v/\partial z$). At $x/h = 6$ (figure 13a), most of the in-plane velocity vectors in the jet column have a magnitude of about 10–50 m s^{-1} and point towards the centre. A symmetric distribution of the transverse velocity field is quite evident. The ω_x contours show distinct vorticity concentrations, suggesting the presence of streamwise vortices. Several studies have reported the presence of stationary streamwise vortices in the mixing-layer region of supersonic jets (Krothapalli, Strykowski & King 1998 and references therein). Novopashin & Perepelkin (1989) and Krothapalli *et al.* (1998) have shown a strong correlation between disturbances originating in the nozzle boundary layer and the presence of streamwise structure in the shear layer downstream. The critical height of the disturbance necessary to trigger the formation of streamwise vortices is quite small ($\delta^*/12$, where δ^* is the nozzle exit boundary-layer displacement thickness). Hence, the unavoidable surface imperfections inside the nozzle will initiate
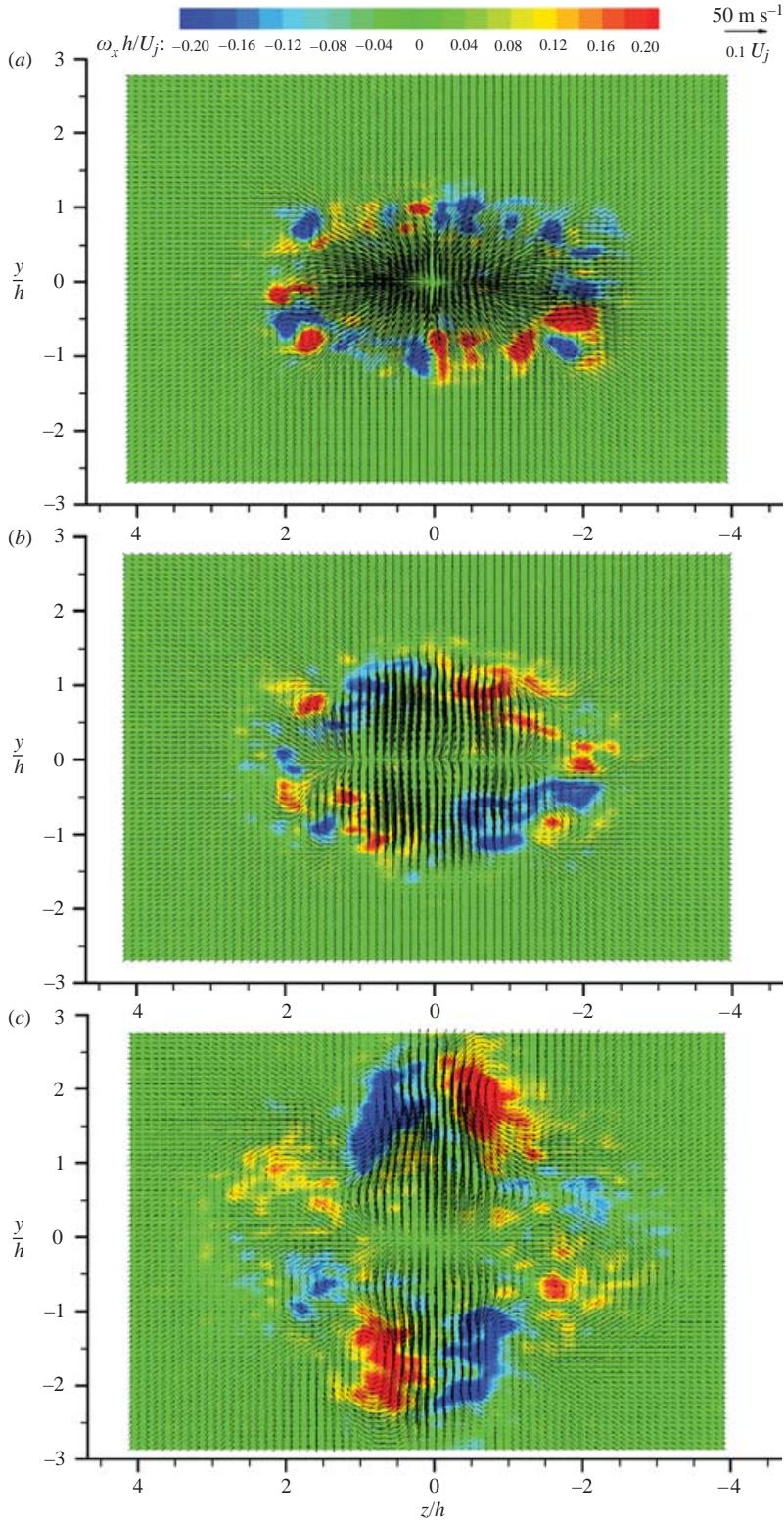
FIGURE 13. Cross-plane transverse mean velocity and vorticity fields. (*a*) $x/h = 6$; (*b*) $x/h = 8$; (*c*) $x/h = 16$.
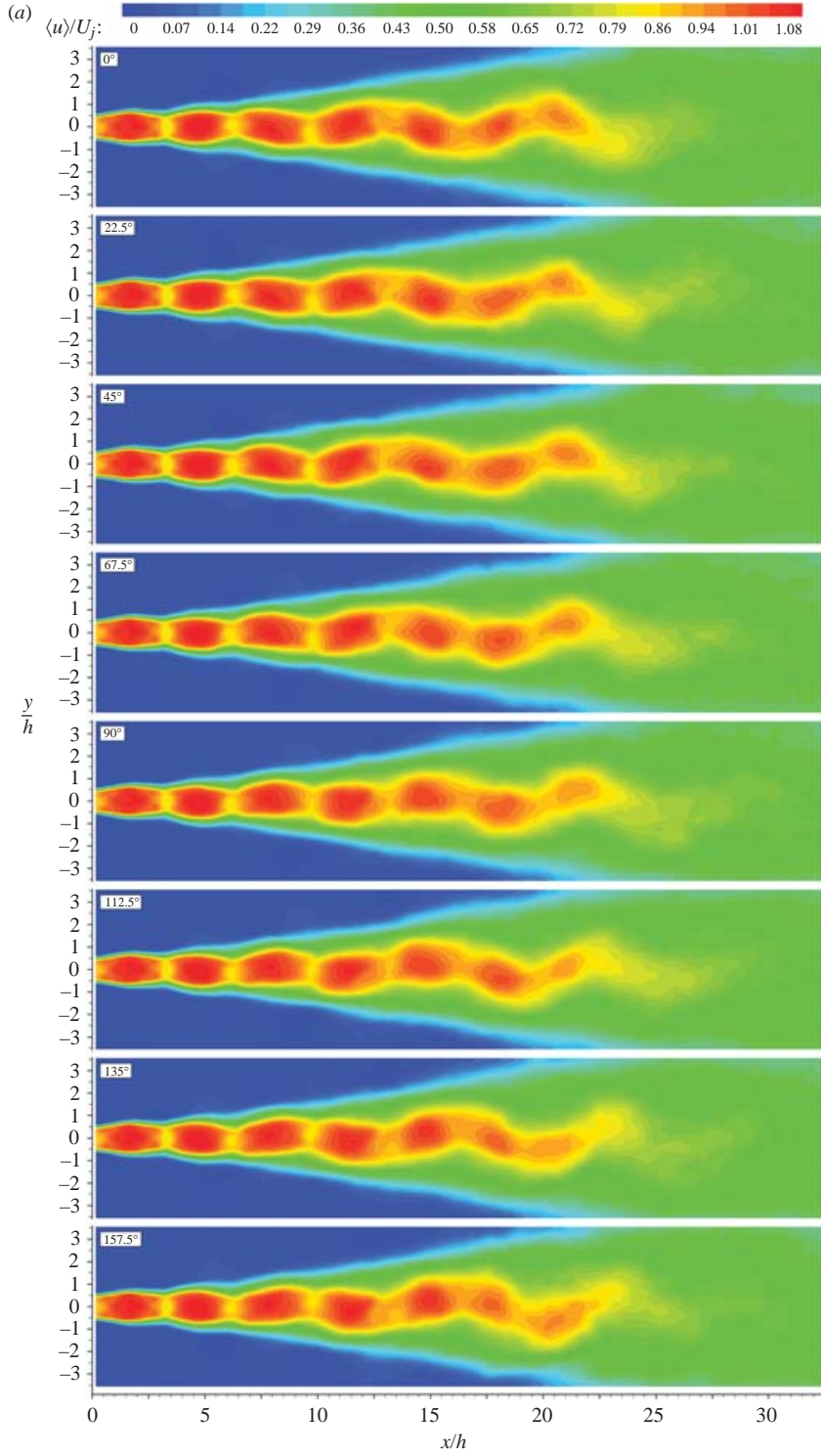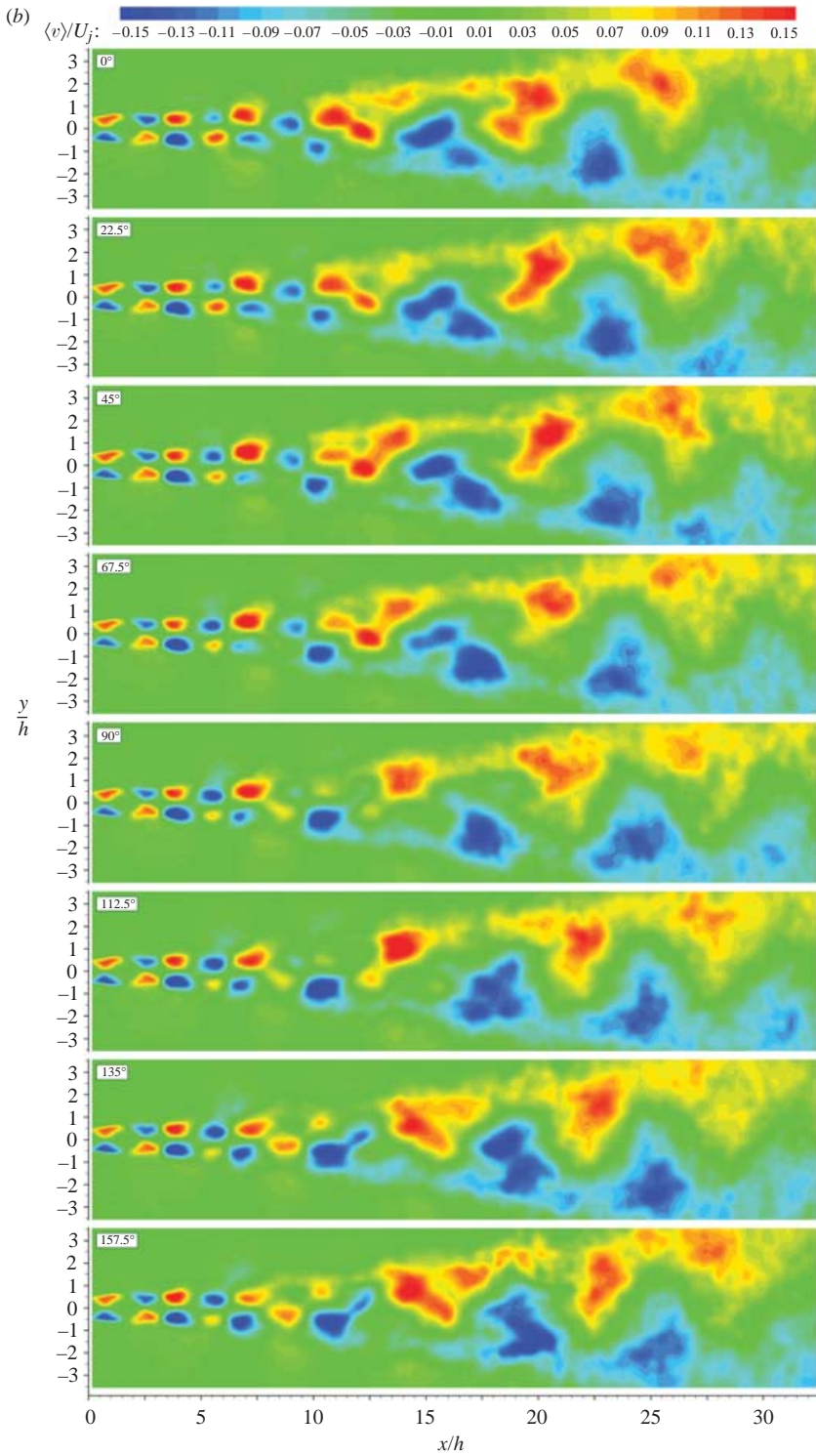
FIGURE 14(*a*). For caption see facing page.

FIGURE 14. (*a*) The phase-averaged axial velocity field and (*b*) the phase-averaged transverse velocity field, during half of the screech cycle.

the streamwise vortices shown in the figure. These vortices once formed, grow very rapidly in the curved shear layer because of the instability Taylor–Görtler type seen in figure 13(*b*).

Further downstream at $x/h = 16$ (figure 13*c*), strong concentrations of streamwise vorticity accompanied by two counter-rotating vortex pairs dominate the flow field. Also seen in figure 13(*c*) is a reminder of the corner vortices. While studying the dynamics of an elliptic jet under a controlled longitudinal excitation to induce periodic formation of vortical structures ('rolls'), Husain & Hussain (1993) observed similar streamwise structures and named them 'ribs'. They have been deduced primarily from numerical simulations guided by experimental results. In our experiment, the spanwise structures are generated by the self-excitation and their three-dimensional deformation leads to the fixed streamwise vortices. For the detailed 'rib' formation mechanism, refer to Husain & Hussain (1993). These streamwise vortices will enhance the transverse transport between the jet and the surrounding fluid there by promoting the axis switching seen in rectangular jets. Indeed, the absence of axis switching in ideally expanded rectangular jets (Krothapalli *et al.* 2003) is primarily due to lack of coherent spanwise vortices. However, such a jet can be made to switch axes if it is excited to induce periodic formation of coherent vortices like those seen in figure 1. Similarly, screech suppression will result in a jet development similar to that of an ideally expanded jet without the cross-over phenomenon.

3.3. *Mean flow at constant phase*

In this section, the velocity field data in the central minor-axis plane are used to discuss the coherent structure properties. Although, the jet development becomes three-dimensional beyond $x/h = 10$, it is possible to extract meaningful coherent structure dynamics in the central plane, as discussed below. Figures 14(*a*) and 14(*b*) show the axial, $\langle u \rangle$ and transverse velocity $\langle v \rangle$ contours in the central minor-axis plane at eight different phases during half of the screech cycle. The second half of the screech cycle simply repeats the data after reflection of each figure in the plane of symmetry (see figure 5). The axial velocity contours clearly show the shock cell structure with a distinct demarcation between the high- and low-speed regions. In addition, the shock cells oscillate, signifying the well-known character of the flapping mode. These oscillations are small in amplitude at the jet exit and increase with downstream distance. The corresponding transverse velocity contours, shown in figure 14(*b*), show vividly the effect of the oscillatory nature of the flow in the shear layer surrounding the shock cell structure. The magnitude of the *v*-component velocity observed is about $\pm 0.15\, U_j$. The flapping mode of the jet is clearly depicted by the asymmetric distribution of the transverse velocity contours for $x/h > 7.5$. The shear layer surrounding the first few shock cells shows symmetric transverse velocity contours, suggesting that a symmetric oscillatory mode is dominant. Using signals from microphones located symmetrically on either side of a screeching rectangular jet, Shih, Krothapalli & Gogineni (1992) observed the presence of simultaneous symmetric and antisymmetric or flapping modes. However, the frequency of the oscillation as measured by a near-field microphone in the present experiment corresponds only to the flapping mode of the jet.

The large-scale vortical structures seen in figure 1 can be deduced by examining the mean vorticity at constant phase, $\langle \omega_z \rangle = \partial \langle v \rangle / \partial x - \partial \langle u \rangle / \partial y$ as shown in figure 15. The vorticity contours seen in the figure are a clear indication of the presence of large-scale coherent vortical structures. The vortical structures are highly three-dimensional in nature and as a result, the vorticity contours appear to be fragmented. The source of
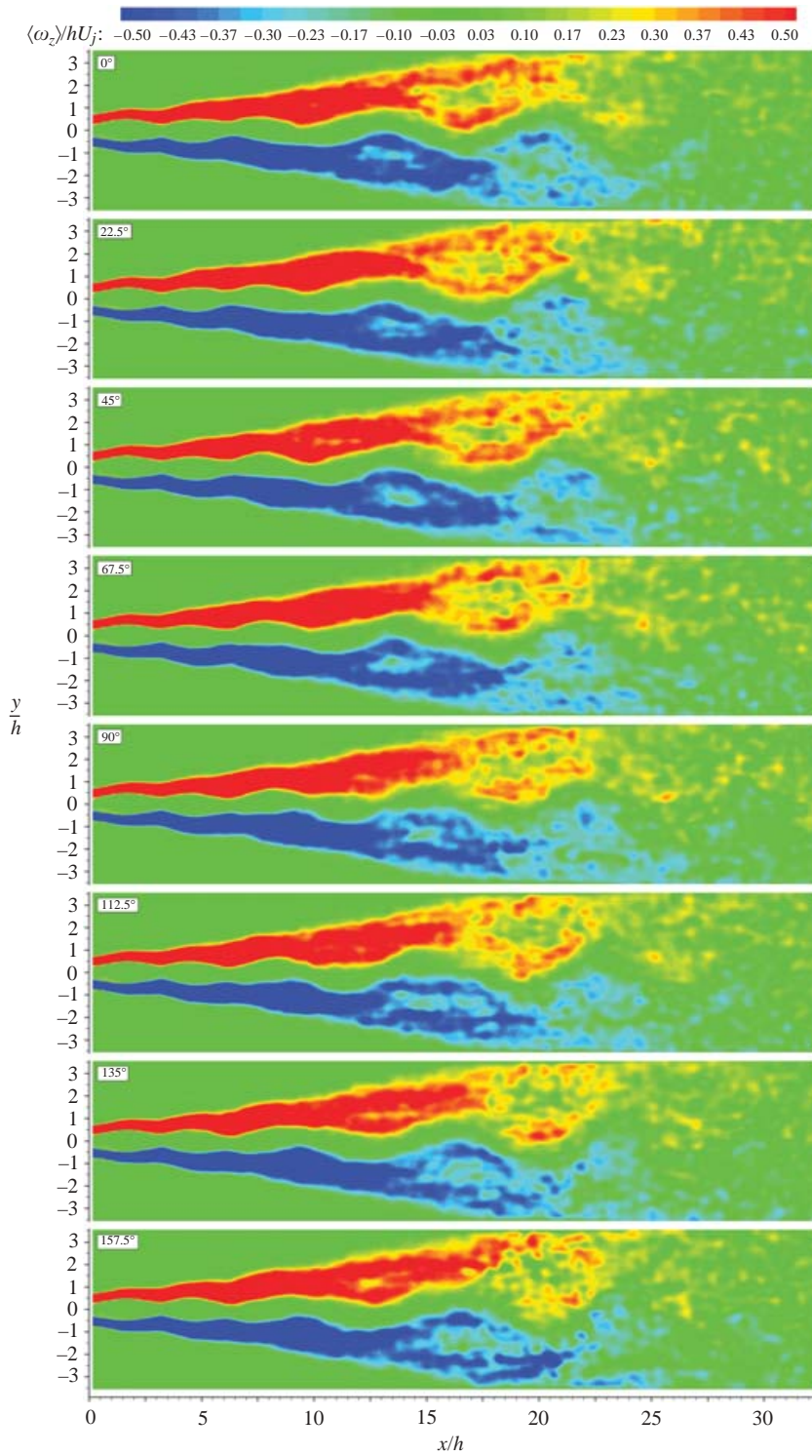
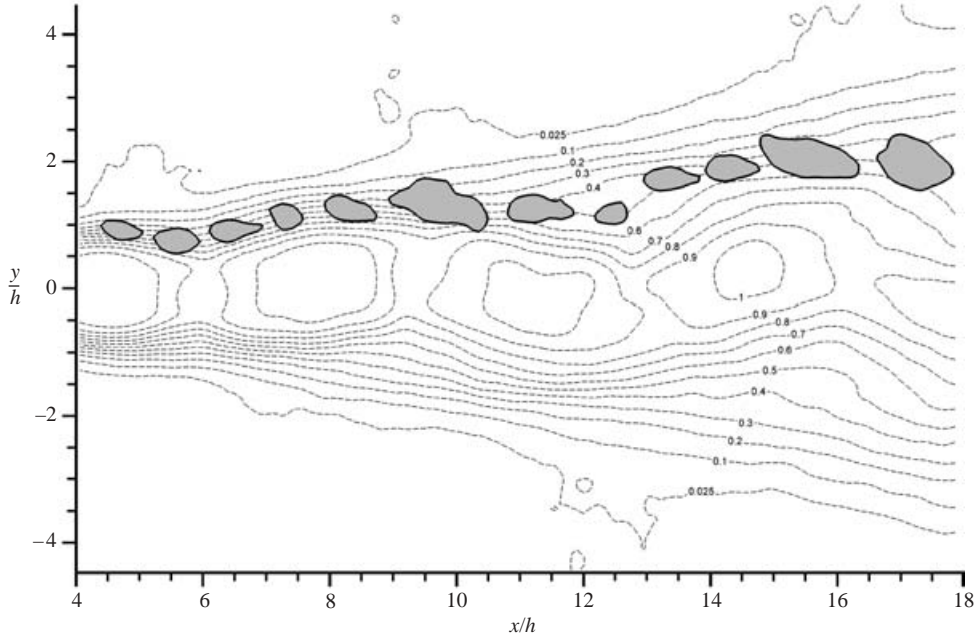FIGURE 15. Phase-averaged vorticity corresponding to the velocity fields shown in figure 14.

FIGURE 16. The coherent structure size determination through R_{uu} spatial correlation distribution along the shear layer at $u = 0.5\,U_j$, $M_j = 1.69$, phase 135°. ——, $R_{uu} = 0.6$; ---, $\langle u \rangle / U_j$.

three-dimensionality can be attributed to the generation of streamwise vortices in the shear layers as discussed briefly in §3.2.2. These spanwise vortices upon interacting with the compression regions of the shock cell generate intense sound; hence, their strength is likely to play a significant role in determining the sound intensity. It is convenient to introduce the circulation Γ, as a measure of the large-scale vortex strength, which can be determined from the value of the area integral:

$$\Gamma_A(\boldsymbol{x}_0) = \oiint_A \omega_z \, \mathrm{d}A. \tag{12}$$

In the above relation, the boundary of the vortical regions need to be specified correctly to yield a meaningful value for the circulation.

The spatial correlation, R_{uu} as defined by (13) is used to obtain the area representing coherent regions of the vorticity.

$$R_{uu}(\boldsymbol{x}_0, \boldsymbol{x}) = \frac{\displaystyle\sum_{i=1}^{N_m} u''(\boldsymbol{x}_0) \cdot u''(\boldsymbol{x})}{\left(\displaystyle\sum_{i=1}^{N_m} u''(\boldsymbol{x}_0)^2\right)^{1/2} \cdot \left(\displaystyle\sum_{i=1}^{N_m} u''(\boldsymbol{x})^2\right)^{1/2}} \tag{13}$$

In (13), the two terms in the denominator are the r.m.s. values of the random fluctuations of the axial velocity and N_m is the number of realizations at the given phase m. A value of 1 for R_{uu} indicates the maximum possible correlation. Using the instantaneous velocity fields obtained at a given phase of the screeching cycle, the correlated regions of axial velocity are obtained as shown in figure 16. Although it is logically a better choice, because of the variation in shape and location of vortices in
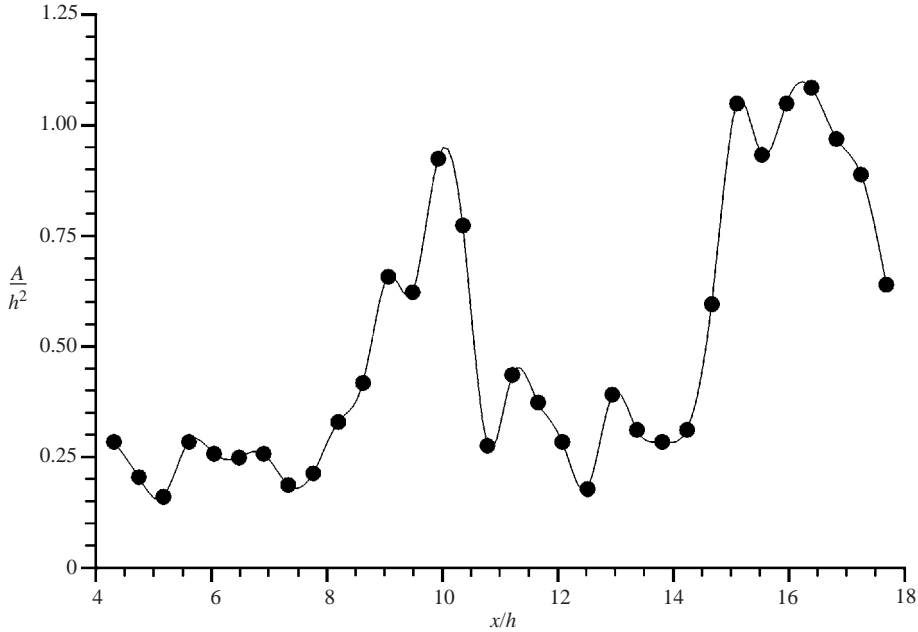
FIGURE 17. The spatially coherent structure size variation along the shear layer at $u = 0.5U_j$, $M_j = 1.69$, phase 135°.

every sample, $R_{\omega\omega}$ did not yield smooth contours as compared to R_{uu}. If there were more samples for each phase, then we expect that $R_{\omega\omega}$ would yield similar results.

The results shown in figure 16, correspond to the velocity field at a typical phase of 135°. The positions $\boldsymbol{x}_0$ in (13), were chosen in the shear layer at discrete axial locations where $\langle u \rangle = 0.5\,U_j$. The R_{uu} contours, with magnitude ranging from 0.6 to 1, are shown in the figure at only selected positions to avoid overlapping in the figure. The phase-averaged axial-velocity magnitude contours are also shown. In order to observe the variation, the area is determined for each point where $R_{uu} > 0.6$ and plotted in figure 17. Two downstream locations, $x/h = 10.5$ and $x/h = 17.5$, indicate large areas suggestive of large-scale spatially coherent vortical structures. The circulation calculations were then performed within the shaded regions shown in figure 16 using equation (12). The magnitude of the circulation is appropriately normalized using h and U_j, and it is plotted in figure 18. Also shown in the figure are data from a jet operating away from the maximum screeching condition. Two distinct peaks can be identified at axial distances of about $10.5\,h$ and $17.5\,h$ corresponding to the large structures at the end of the third and fifth shock cells. The strength of the large structure determined by its circulation magnitude is highest at the end of the third shock cell and it corresponds to the location of the generation of the intense sound. The circulation magnitudes of the structures at $M_j = 1.74$ show lower levels, suggesting lower-strength vortical structures.

Since the locations and sizes of the vortical structures are identified, it is also possible to use this information to calculate the convective speed of these structures. The vorticity weighted average of the velocity field within the area as suggested by Shih, Lourenco & Krothapalli (1995)

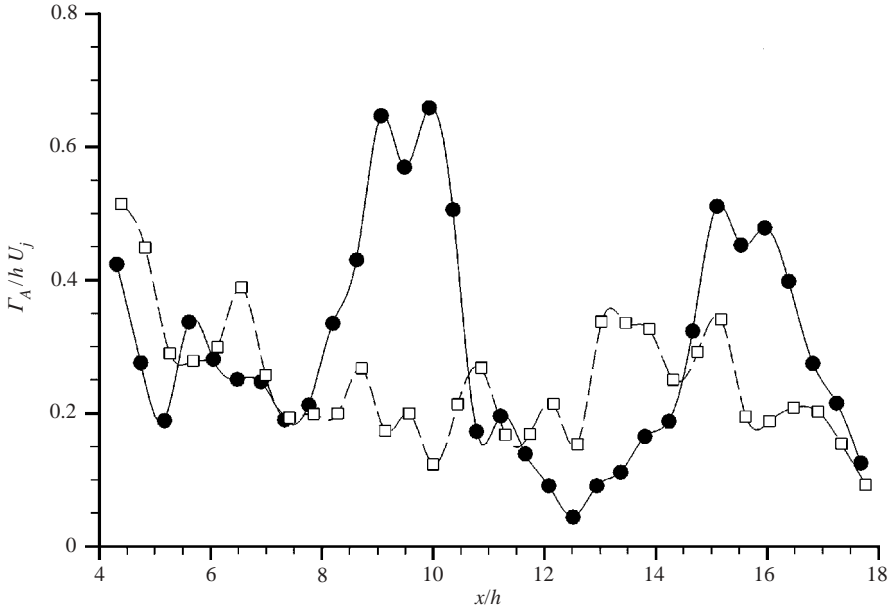$$\boldsymbol{u}_c = \frac{1}{\Gamma_A} \oiint_A \boldsymbol{u}\omega_z \, \mathrm{d}A \qquad (14)$$

FIGURE 18. The variation of the coherent structure circulation with downstream distance for phase 135° ——•——, $M_j - 1.69$; − −□− −, $M_j = 1.74$.

gives a value for the convection velocity of about 0.5 U_j, which is consistent with the previous results obtained using phase-locked schlieren photography (Krothapalli *et al.* 1986). The data show little variation with downstream distance (Alkislar 2001). In estimating the screech frequency, the convection velocities of the large-scale disturbance are taken as a simple constant value and it seems to be borne out from the present experimental results.

3.3.1. *Three-dimensional development: cross-plane mean flow at constant phase*

To elucidate the deformation of the rectangular jet, it is necessary to examine the phase-averaged mean cross-flow field at different downstream locations. Figure 19 shows the uniformly scaled velocity vectors superimposed with the out-of-plane component of the vorticity at three different phases within a screech tone period at $x/h = 12$. The presence of the streamwise vortices often consisting of counter-rotating pairs is seen in these pictures.

Using numerical simulation, Husain & Hussain (1993) have delineated the generation of streamwise vorticity from the coherent spanwise structures. One of the main features of their analysis is the formation of the ribs consisting of streamwise vorticity from the deformation of the elliptic vortex structures similar to those shown here. The strength of the streamwise structures is an order of magnitude lower than that of the spanwise structures as determined by the vorticity magnitude. For example, the normalized maximum vorticity magnitude in figure 15 corresponding to the spanwise structures is about 0.5 as compared to that of 0.01 for the streamwise structures seen in figure 19. The self-induced motions of these streamwise vortices produce a strong transverse outward velocity, as shown in the figure, indicating the outward movement of the jet fluid in the flapping plane and as a consequence the major-axis side is pushed further outward. This action produces higher mixing as suggested by an increase in the spreading rate of the jet in the minor-axis plane.
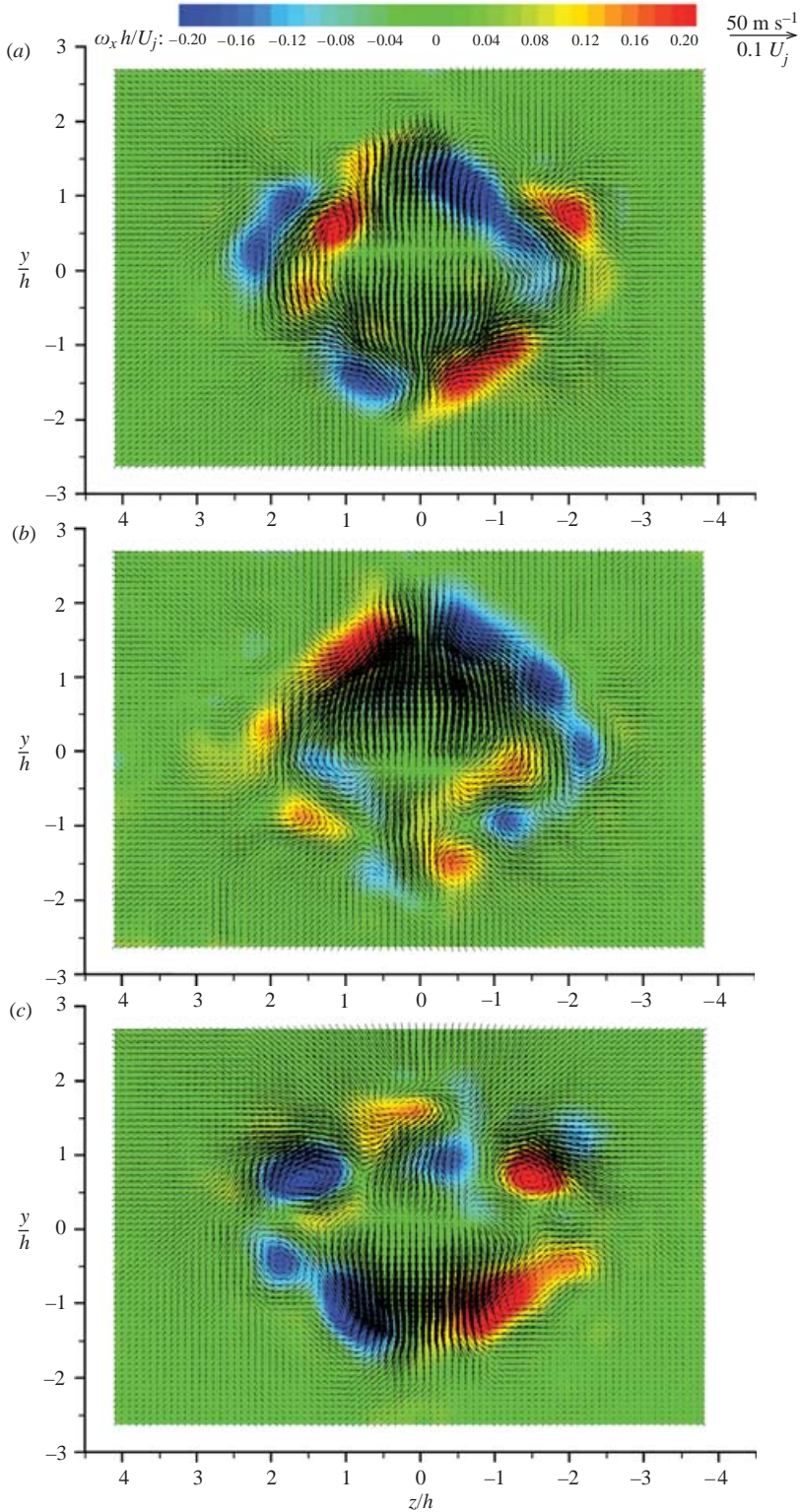
FIGURE 19. Phase averaged cross-plane velocity and vorticity fields at three different phases at $x/h = 12$, (*a*) phase 0°, (*b*) phase 135° and (*c*) phase 270°.
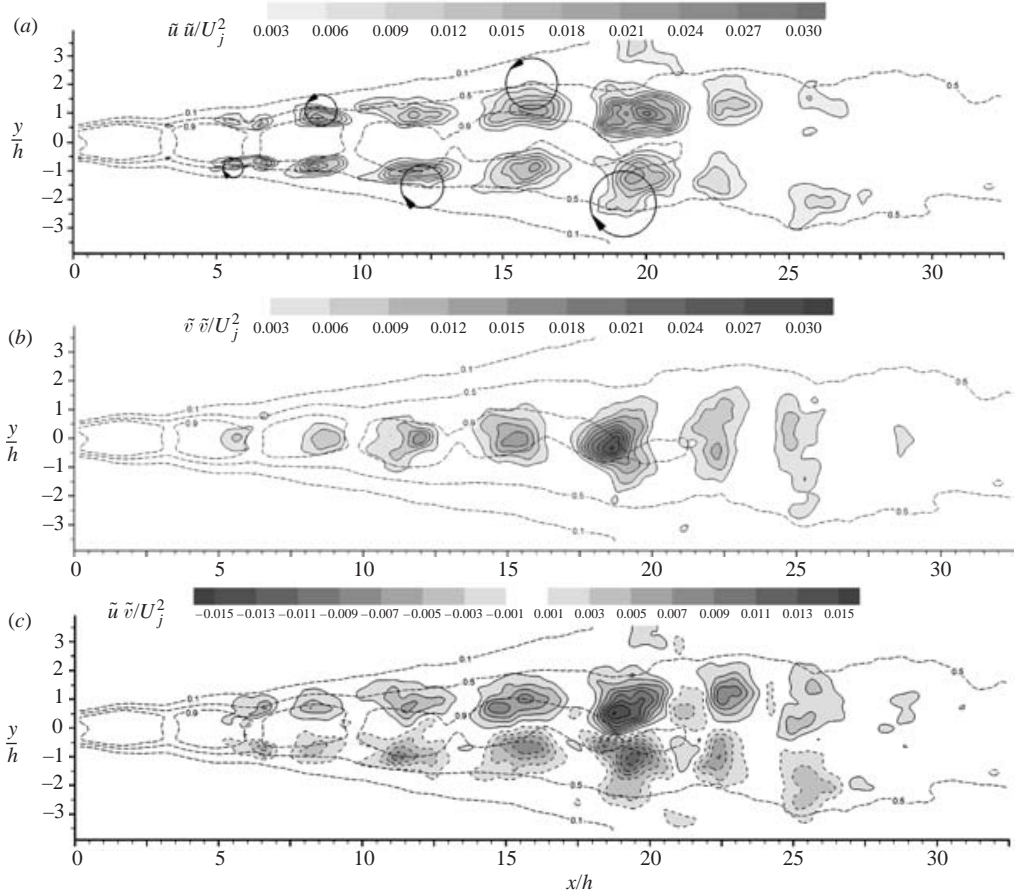
FIGURE 20. Contours for periodic components of the Reynolds stress at constant phase 135°.
(*a*) $\tilde{u}\tilde{u}/U_j^2$; (*b*) $\tilde{v}\tilde{v}/U_j^2$; (*c*) $\tilde{u}\tilde{v}/U_j^2$. ---, u/U_j.

3.4. *Turbulence characteristics*

Since, an important portion of the flow field is periodic in time, the fluctuation away from a global mean $\bar{q}$ consists of a contribution from the periodic large-scale motion $\tilde{q}$ and a contribution q'' from the random fluctuations. When an ensemble of data is considered at a fixed phase, the mean of this ensemble describes the periodic motion $\tilde{q}$, with the vortices stationary at an average location. Fluctuations from the mean value at a fixed phase come from two main sources. In the following discussion, every fluctuation from the mean at constant phase will be considered as random q''. The fluctuations due to the variations in shape and location of the vortices in every sample also contribute to this quantity; however, it is difficult to quantify the amount of the contribution. Reynolds stresses here are associated with both the vortex variations and the random fluctuations of velocity. These spatially resolved stresses at different phases are used in the following discussion.

In figure 20, the three normalized components of the periodic Reynolds stress $\tilde{u}\tilde{u}$, $\tilde{v}\tilde{v}$ and $\tilde{u}\tilde{v}$ are shown in the central minor-axis plane at a typical phase of 135°. The measured area covers a region from the nozzle exit to $32.5\,h$ in the axial direction, and $-3.5\,h$ to $3.5\,h$ in the transverse direction. Recognizing that the flow is highly
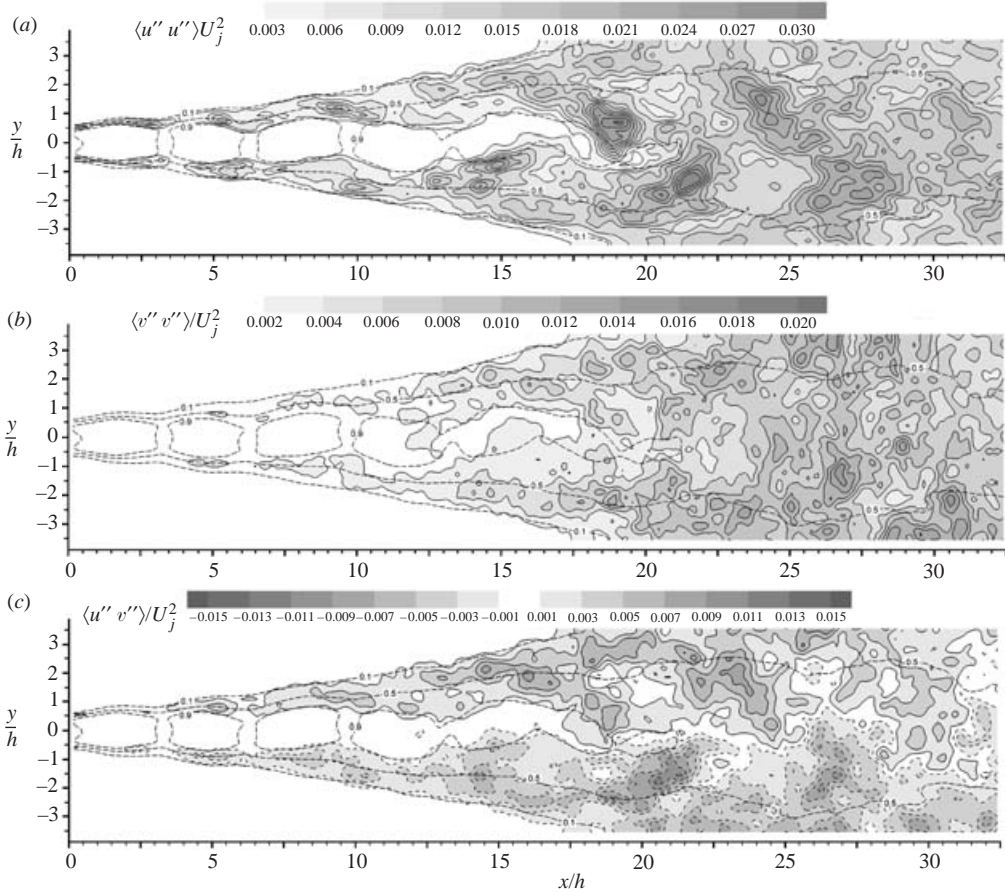
FIGURE 21. Contours for random components of the Reynolds stress at phase 135°.
(a) $\langle u'' u'' \rangle / U_j^2$; (b) $\langle v'' v'' \rangle / U_j^2$; (c) $\langle u'' v'' \rangle / U_j^2$. ---, u/U_j.

three-dimensional, the central plane was chosen to examine the turbulence characteristics, being the most representative of the flow field. The stresses are shown in contour plots with their magnitude represented by the grey scale and the solid and dashed lines denote the positive and negative values, respectively. Included in the figure are the normalized mean velocity contours depicting the boundaries of the shock cells and the shear layer. The locations of the large-scale vortical structures, as obtained from the R_{uu} contours are also included in the figure. The normal stress values show a strong symmetry with respect to the jet centreline. The periodic motion is primarily a consequence of the local transverse motion of the shock cells with respect to the global mean, which generates peaks in $\tilde{u}\tilde{u}$ on either side of the shock cell structure. Typical normalized peak values in the shear layer are found to be about 0.02. The maximum normalized value of $\tilde{u}\tilde{u}$ is found to be 0.025 at $x = 20h$ and $y = 1h$, which corresponds to the location where the shock cell structure terminates. The other direct result of oscillating shock cells is the sequence of $\tilde{v}\tilde{v}$ peaks along the centreline of the jet with magnitudes comparable to that of $\tilde{u}\tilde{u}$. The normalized maximum value for the transverse periodic normal stress is observed at $x = 18.5h$ with a magnitude of 0.027. The corresponding r.m.s. velocities are about 15% of the mean jet exit velocity. As expected, the periodic shear stress $\tilde{u}\tilde{v}$ distribution exhibits
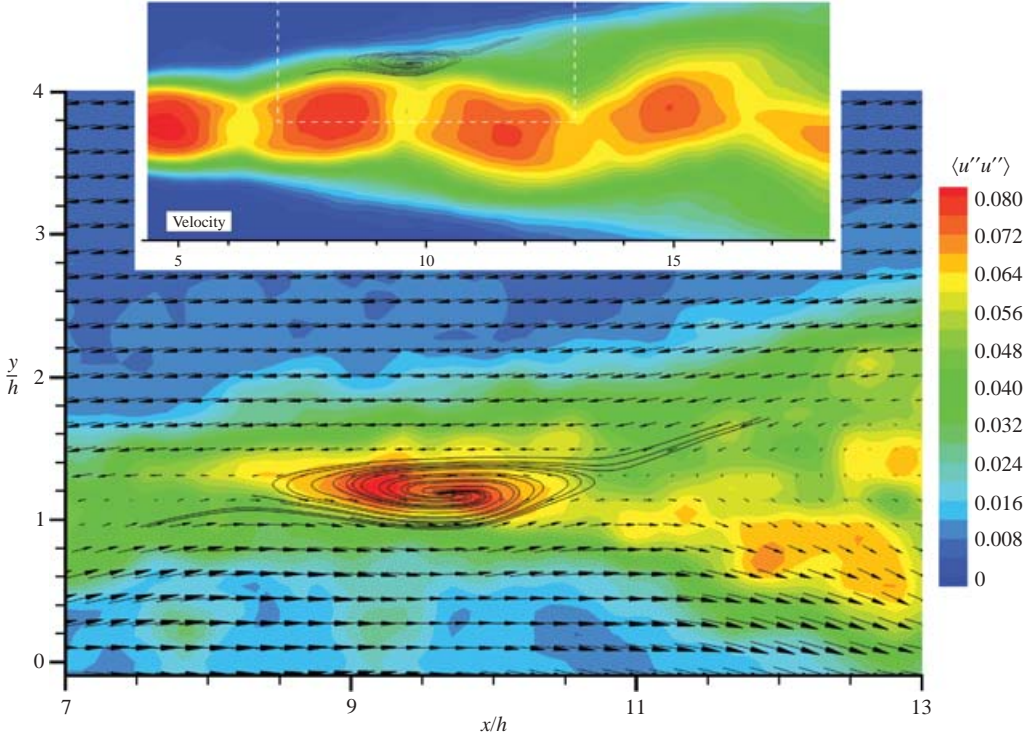
FIGURE 22. The velocity field at a constant phase of $135°$ as viewed from a reference frame moving downstream at $0.5 U_j$. The colour contour represents the magnitude of $\langle u''u'' \rangle$ superimposed with streamlines.

asymmetry about the centreline, with its maximum normalized value being 0.015 at $x = 18.5h$. The magnitudes of these periodic stresses decrease rapidly after about $20h$.

The quantity $\tilde{u}\tilde{u}$ is found to be confined mostly to the high-speed side of the shear layer and it is nearly zero at the centre of the jet. However, the contours of $\tilde{v}\tilde{v}$ are concentrated at the centre of the jet owing to the flapping motion of the shock cells. Unlike in low-speed jet and wake flows (Husain & Zaman 1981; Cantwell & Coles 1983) the periodic shear stress contours do not show alternating character (positive along the top shear layer and negative along the bottom shear layer) except in the far downstream locations of the jet $(x/h > 20)$. Since $\tilde{u}\tilde{u}$ and $\tilde{u}\tilde{v}$ contours are confined mostly to the high-speed side of the shear layer, it is suggested that the periodic stresses are largely a consequence of the flapping motion of the shock cells. The arrangement of the stress contours appears to coincide with the large-scale coherent structure locations with the vortex centres typically aligned with the half-velocity points in the shear layer.

Figure 21 shows the random components of the Reynolds stresses $\langle u''u'' \rangle$, $\langle v''v'' \rangle$ and $\langle u''v'' \rangle$ corresponding to conditions in figure 20. The fluctuation levels due to random turbulence are comparable to the fluctuation levels due to large-scale periodic motions. However, the highest values of the random components are measured at the end of the potential core downstream of about $16h$, where the shear layers on either side of the shock cells merge. The quantities $\langle u''u'' \rangle$, $\langle v''v'' \rangle$ and $\langle u''v'' \rangle$ have normalized maximum values of 0.034, 0.015 and 0.012, respectively. Unlike the periodic Reynolds stresses, the random components are widely spread in the mixing region downstream
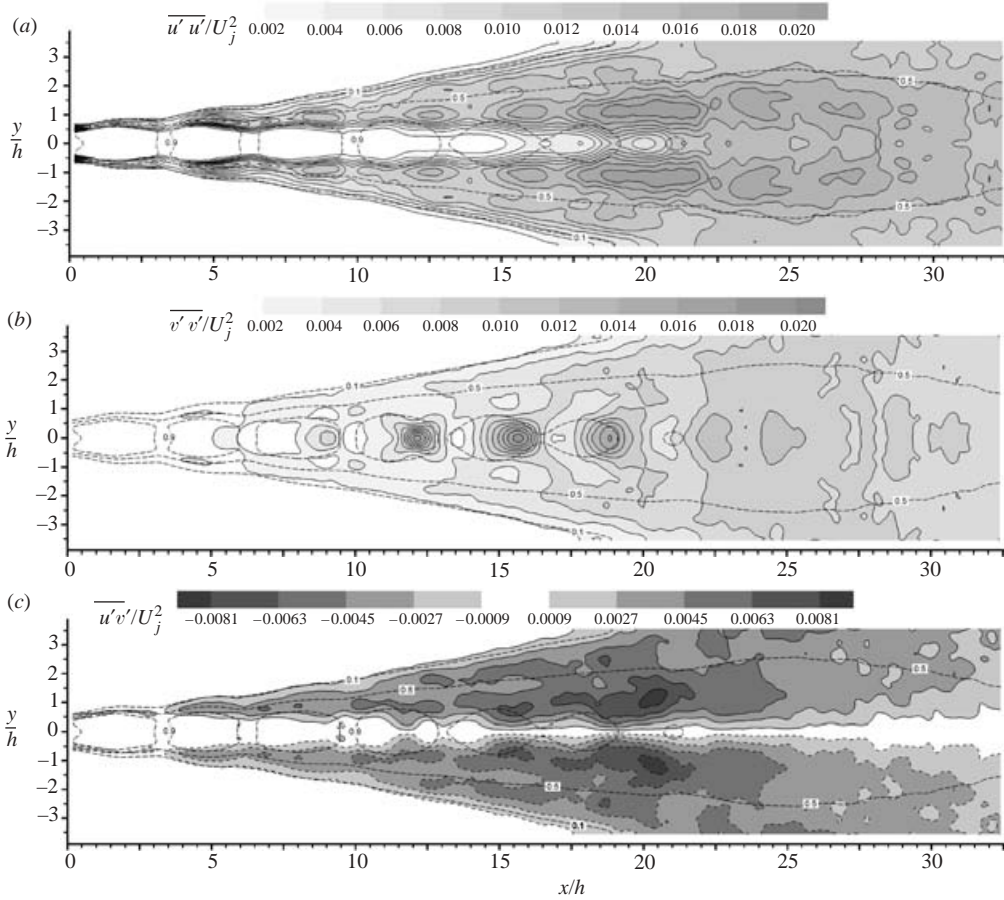
FIGURE 23. Contours for global mean components of the total Reynolds stress.
(*a*) $(\overline{\tilde{u}\tilde{u}} + \langle\overline{u''u''}\rangle)/U_j^2$; (*b*) $(\overline{\tilde{v}\tilde{v}} + \langle\overline{v''v''}\rangle)/U_j^2$; (*c*) $(\overline{\tilde{u}\tilde{v}} + \langle\overline{u''v''}\rangle)/U_j^2$. ---, u/U_j.

of the end of the shock cells. The values of these stresses, although small in the shear layers, appear both in the high- and low-speed sides. This is in contrast to the periodic Reynolds stresses, $\tilde{u}\tilde{u}$ and $\tilde{u}\tilde{v}$, which are confined only to the high-speed side of the shear layer. Since the random stresses have nearly zero values within the shock cell structure, any phase jitter arising from the irregularity of the large-scale motions in the jet has not seriously affected the measurements of Reynolds stresses due to random turbulence.

On close examination of the vorticity field, it appears that the peak location of the random Reynolds stresses is coincident with the positions of the large-scale vortices. A vivid presentation of this observation is seen in figure 22, where the expanded velocity field at the end of the third shock cell is superimposed with the $\langle u''u''\rangle$ contours along with the streamline pattern at phase 135°. The convective velocity of the vortical structure is subtracted from the whole flow field. The shock cell pattern is shown in the inserted figure with the coloured contours of the axial velocity magnitude. The vortical structure is captured at the end of third shock cell by the R_{uu} contours shown in figure 16. Shown in this fashion, it is clear that the vortex location coincides with the peak in the random normal stress. Similar observations were made by Husain & Zaman (1981) at very low-speed jet flows.
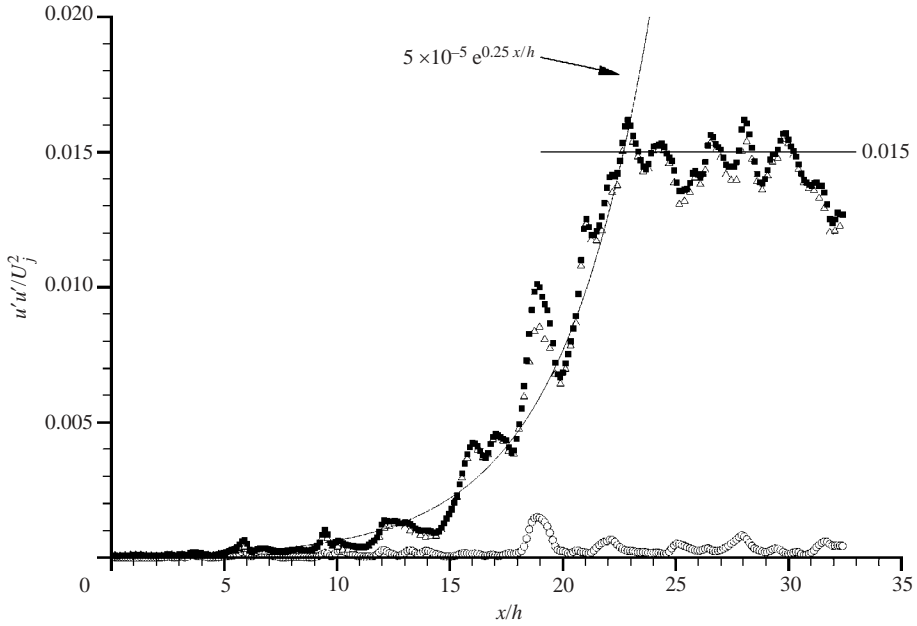
FIGURE 24. The variation of streamwise mean Reynolds normal stress along the centreline.
$\circ$, $\tilde{u}\tilde{u}/U_j^2$; $\triangle$, $\overline{u''u''}/U_j^2$; $\blacksquare$, $\overline{u'u'}/U_j^2$.

The global mean periodic and random Reynolds stress components (e.g. $\overline{\tilde{u}\tilde{u}}$ and $\langle\overline{u''u''}\rangle$), averaged over one screech cycle, show results that are quite similar to those seen in figures 20 and 21 (Alkislar 2001). For the sake of brevity, they are not included here. However, the global mean total Reynolds stress components (e.g. $\overline{u'u'}$) are given in figure 23. These quantities are the conventional stresses obtained by classical Reynolds averaging (given that the flow is treated as statistically stationary). They can be calculated by simply adding the two components of the global mean stresses (e.g. $\overline{u'u'} = \overline{\tilde{u}\tilde{u}} + \langle\overline{u''u''}\rangle$). The $\overline{u'u'}$ contours show that the streamwise normal stresses assume higher values at the high-speed side of the shear layer with local maximums at the shock cell ends adjacent to the shock cell boundary. At $19\,h$ a value of 0.021 is observed corresponding to a normalized turbulence intensity of 0.145.

The transverse total Reynolds normal stress shows the dominant character of the periodic components over the entire flow field. The maximum level is achieved at $16\,h$ with a value of 0.019. The corresponding turbulence intensity for the transverse velocity fluctuations is 0.14, which is comparable to the streamwise turbulence intensity. Finally, the global mean total Reynolds shear stress is shown in figure 23(c). The combined effect of turbulent and periodic shear stresses is felt mostly in the region where the merging of the two shear layers occurs. A peak value of 0.0086 is observed at $20.5\,h$, after which the fluctuations begin to reduce, as will be shown in the distribution of centreline turbulence intensities.

The variation of $\overline{u'u'}$ along the centreline is given in figure 24. The data clearly shows the rapid (exponential) increase of the fluctuations along the jet centreline as represented by the solid curve, starting with a relatively low value of 0.0001 corresponding to turbulence intensity of 0.01, to reach a maximum value of about 0.015 at $23\,h$. Also included in the figure are the corresponding periodic and random components. Consistent with previous observations discussed above, the
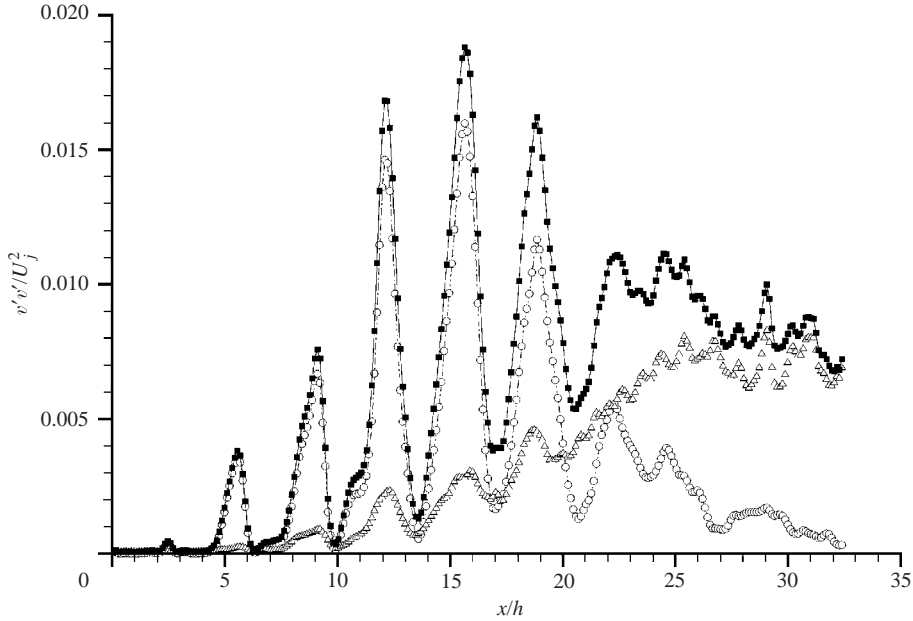
FIGURE 25. The variation of transverse mean Reynolds normal stress along the centreline.
○, $\tilde{v}\tilde{v}/U_j^2$; △, $v''v''/U_j^2$; ■, $v'v'/U_j^2$.

random fluctuations are dominant over the periodic fluctuations along the centreline, suggesting that there is no significant periodic movement of shock cells in the axial direction.

In figure 25, the variation in $\overline{v'v'}$ along the centreline is shown. In contrast to $\overline{u'u'}$, the variation in the transverse global mean Reynolds normal stress is dominated mostly by the periodic fluctuation up to the end of the potential core. The maximum value is observed at the location of the fifth shock cell ($x/h = 15$). At about $x/h = 20$, the magnitude of the periodic component decreases precipitously and the random fluctuations begin to increase. The modulation of the transverse fluctuation intensities within the shock cell is very significant (within the fifth shock cell, the fluctuation intensity changes between the values of 0.035 and 0.14), indicative of the strong flapping motion of the jet column. The sudden breakdown of the turbulence energy associated with the periodic component at $x/h = 20$, is clearly depicted in the distribution of the normal stresses in the shear layer at half-velocity points as shown in figures 26 and 27. In the shear layer, the fluctuations of the random component are of the same order of magnitude as the periodic component. At the end of the supersonic core of the jet, the turbulence intensities begin to decrease as shown in the figure. Beyond $x/h > 20$, the jet is expected to show characteristics similar to that of a subsonic jet.

The turbulence measurements discussed in this section clearly show that a significant part (50%) of the turbulent energy is produced by the periodic large-scale structures in the noise-producing region of the supersonic jet ($0 < x/h < 20$). The maximum values for the periodic and random components of the Reynolds stress seem to be aligned with concentrations of the coherent vorticity, suggesting that the production of turbulent kinetic energy is associated with the unsteady flow generated by the large periodic structures. Suppression of the mechanism that generates these large structures
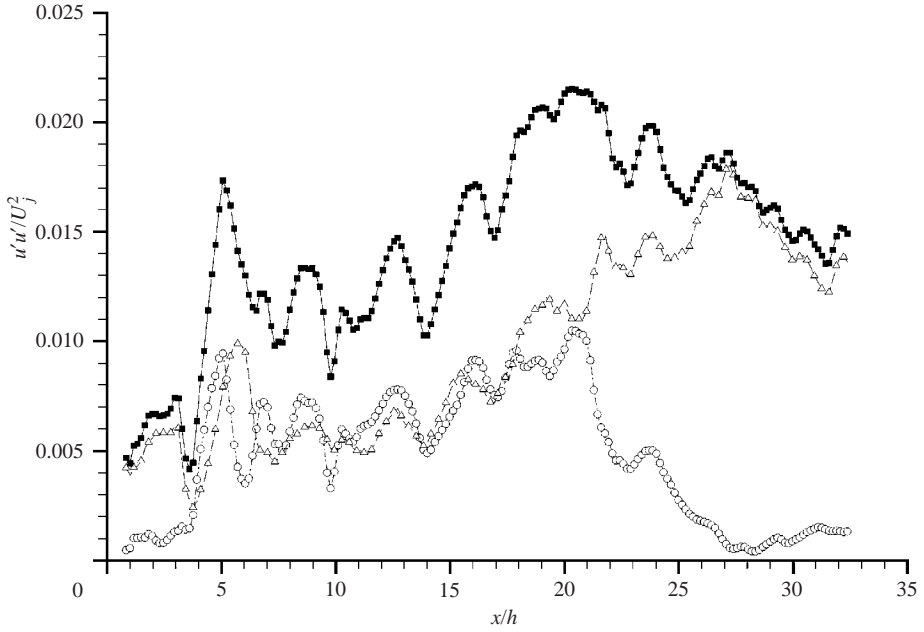
FIGURE 26. The variation of streamwise mean Reynolds normal stress along the shear layer. $\bigcirc$, $\tilde{u}\tilde{u}/U_j^2$; $\triangle$, $u''u''/U_j^2$; $\blacksquare$, $u'u'/U_j^2$.
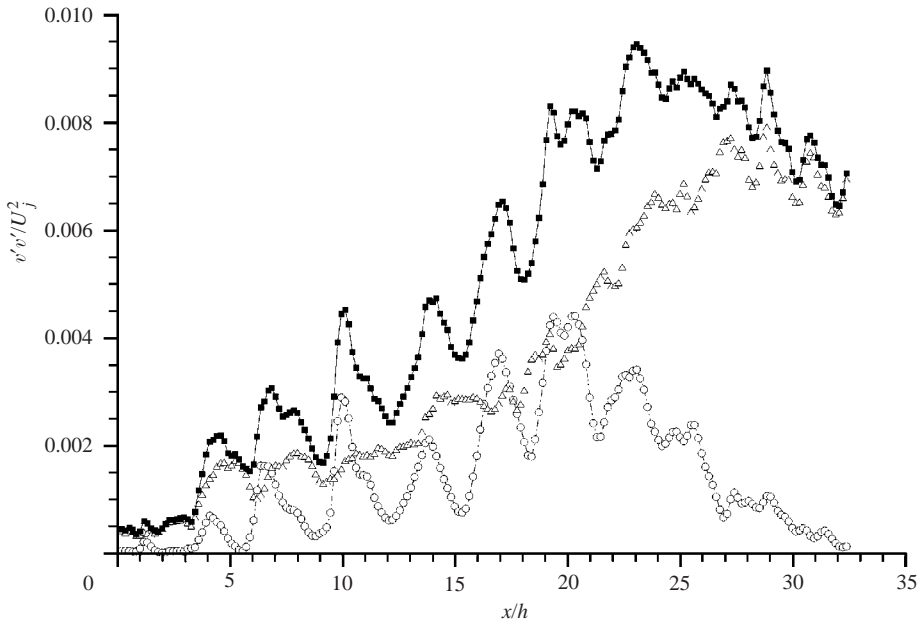

FIGURE 27. The variation of transverse mean Reynolds normal stress along the shear layer. $\bigcirc$, $\tilde{v}\tilde{v}/U_j^2$; $\triangle$, $v''v''/U_j^2$; $\blacksquare$, $v'v'/U_j^2$.

may result in turbulence suppression which leads to far-field noise reductions. Indeed, our attempts to accomplish this task with microjet air/water injection show promising results (Krothapalli, Greska & Arakeri 2002).

4. Conclusions

The three-dimensional flow characteristics of a screeching rectangular jet are explored using a relatively new experimental technique, stereoscopic particle image velocimetry. The three-dimensional evolution of the rectangular jet with its distinctive character of the cross-over phenomenon (switching of the jet major and minor axes) is captured. The absence of the cross-over phenomenon in ideally expanded rectangular and elliptic jets, that is so prevalent in low-speed jets, was somewhat puzzling. The present experimental results show that the three-dimensional deformation of the large-scale spanwise coherent vortical structures results in strong streamwise vortices that are responsible for the axis-switching phenomenon. The periodic formation of the large-scale spanwise structures in a screeching jet is due to self-excitation. It is believed that such structures can be generated in an ideally expanded jet if a controlled longitudinal excitation is imposed at the nozzle exit. Husain & Hussain (1993), using experimental and numerical simulations of low-speed elliptic jets, admirably describe the mechanism for the generation of the streamwise vortices.

The dynamics of the coherent eddies are studied via the temporal evolution of their circulation. At the maximum screeching condition, strong coherent vortical structures are found to dominate the shear layer in the region of the screech sound generation. The flow-field measurements, in conjunction with the schlieren pictures, suggest that the birth of the acoustic wave associated with the screech tone results from relatively high turbulent fluctuations in the shear layer at the end of a shock cell. These fluctuations are due to the interaction of intense concentration of vorticity associated with a large-scale coherent structure with the shock cell. Accordingly, at conditions where the screech is weaker, such intense vortical structures are not observed. It is concluded that the presence of coherent vorticity of significant strength, in addition to the shock cell strength, is largely responsible for determining the intensity of the screech. Reduction in either of these parameters will result in reductions in screech amplitude.

Using the well-known triple decomposition of the velocity, it is found that the turbulent energy for $x/h \leqslant 20$, consists of contributions from both the periodic large-scale and chaotic small-scale turbulence. The turbulence energy associated with the periodic motion of the jet drops precipitously at the location where the streamwise vortical structures become prominent.

REFERENCES

ALKISLAR, M. B. 2001 Flow field measurements in a screeching rectangular jet. Dissertation, Florida State University, Tallahassee.

ALKISLAR, M. B., LOURENCO, L. M. & KROTHAPALLI, A. 2000 Stereoscopic PIV measurements of a screeching supersonic jet. *J. Visualization* **3**, 135–143.

BERMAN, C. H. & FFOWCS WILLIAMS, J. E. 1970 Instability of a two-dimensional compressible jet. *J. Fluid Mech.* **42**, 151–159.

BROCHER, E. & MAKHSUD, A. 1997 A new look at the screech tone mechanism of underexpanded jets. *Eur. J. Mech. B/Fluids* **16**, 877–891.

CANTWELL, B. & COLES, D. 1983 An experimental study of entrainment and transport in the turbulent near wake of a circular cylinder. *J. Fluid Mech.* **136**, 321–374.

HUSAIN, H. S. & HUSSAIN, F. 1993 Elliptic jets. Part 3. Dynamics of preferred mode coherent structure. *J. Fluid Mech.* **248**, 315–361.

HUSAIN, H. S. & ZAMAN, K. B. M. Q. 1981 The 'preferred mode' of the axisymmetric jet. *J. Fluid Mech.* **110**, 39–71.

KROTHAPALLI, A., BAGANOFF, D. & HSIA, Y. 1983 On the mechanism of screech tone generation in underexpanded rectangular jets. *AIAA Paper* 83-0727.

KROTHAPALLI, A., BAGANOFF, D. & KARAMCHETI, K. 1981 On the Mixing of a Rectangular Jet. *J. Fluid Mech.* **107**, 201–220.

KROTHAPALLI, A., GRESKA, B. & ARAKERI, V. 2002 High speed jet noise reduction using microjets. *8th AIAA/CEAS Aeroacoustics Conf. AIAA Paper* 2002-2450.

KROTHAPALLI, A., HSIA, Y., BAGANOFF, D. & KARAMCHETI, K. 1986 The role of screech tones on mixing of an underexpanded jet. *J. Sound Vib.* **106**, 119–143.

KROTHAPALLI, A. & STRYKOWSKI, P. J. 1996 Revisiting screech tones: effects of temperature. *AIAA Paper* 96-0644.

KROTHAPALLI, A., STRYKOWSKI, P. J. & KING, C. J. 1998 Origin of streamwise vortices in supersonic jets. *AIAA J.* **36**, 869–872.

KROTHAPALLI, A., VENKATAKRISHNAN, L., LOURENCO, L. & ELAVARASAN, R. 2003 Turbulence and noise suppression of a high-speed jet by water injection. *J. Fluid Mech.* (in press).

LOURENCO, L. & KROTHAPALLI, A. 2000 True resolution PIV: a mesh-free second-order accurate algorithm. *Proc. 10th Intl Symp. on Applications of Laser Techniques in Fluid Mech. Lisbon, Portugal.*

MANNING, T. A. & LELE, S. K. 2000 A numerical investigation of sound generation in supersonic jet screech. *AIAA Paper* 2000-2081.

MORRIS, P. J., GIRIDHARAN, M. G. & LILLEY, G. M. 1990 On the turbulent mixing of compressible free shear layers. *Proc. R. Soc. Lond.* A **431**, 219–243.

NOVOPASHIN, S. A. & PEREPELKIN, A. L. 1989 Axial symmetry loss of a supersonic perturbed jet. *Phys. Lett.* A **135**, 290–293.

PINCKNEY, S. Z. 1975 A short static-pressure probe design for supersonic flow. *NASA TN* D-778.

POLDERVAART, L. J. 1976 Teskst behorende bij de film "Sound pulse-boundary layer interaction studies", Tecnische Hogeschool Eindhoven.

POLDERVAART, L. J., WIJNANDS, A. P. J. & BRONKHORST, L. 1974 Aerosonic games with the aid of control elements and externally generated pulses. *Noise Mechanisms, AGARD CP* **131**, 20.1–20.4.

POWELL, A. 1953 On the mechanism of choked jet noise. *Proc. Phys. Soc. Lond.* **66**, 1039–1056.

PRANDTL, L. 1952 *Essentials of Fluid Dynamics*, pp. 50–51. Blackie.

RAMAN, G. 1998 Advances in understanding supersonic screech: review and perspective. *Prog. Aerospace Sci.* **34**, 45–106.

REYNOLDS, W. C. & HUSSAIN, A. K. M. F. 1972 The mechanics of an organized wave in turbulent shear flow. Part 3. Theoretical models and comparisons with experiments. *J. Fluid Mech.* **54**, 263–288.

SHIH, C., KROTHAPALLI, A. & GOGINENI, S. P. 1992 Experimental observations of instability modes in a rectangular jet. *AIAA J.* **30**, 2388–2394.

SHIH, C., LOURENCO, L. & KROTHAPALLI, A. 1995 An experimental investigation of the flow at leading and trailing edges of a pitching airfoil. *AIAA J.* **33**, 1369–1376.

STRYKOWSKI, P. J., KROTHAPALLI, A. & JENDOUBI, S. 1996 The effect of counterflow on the development of a compressible shear layer. *J. Fluid Mech.* **308**, 63–96.

TAM, C. K. W. 1988 The shock-cell structures and screech tone frequencies of rectangular and non-axisymmetric supersonic jets. *J. Sound Vib.* **121**, 135–147.

YU, K. H. & SCHADOW, K. C. 1994 Cavity-actuated supersonic mixing and combustion control. *Combust. Flame* **99**, 295–301.

WISHART, D. 1995 The structure of a heated supersonic jet operating at design and off design conditions. Dissertation, Florida State University, Tallahassee.